The carbon dioxide removal potential of cement and lime kiln dust via ocean alkalinity enhancement

Gunter Flipkens[1*], Greet Lembregts[1] and Filip J.R. Meysman[1]

[1]Geobiology, Department of Biology, University of Antwerp, Antwerp, Belgium

5 *Correspondence to*: Gunter Flipkens (Gunter.Flipkens@uantwerpen.be)

Abstract. Ocean alkalinity enhancement (OAE) is a proposed method for atmospheric carbon dioxide removal (CDR), and involves the addition of alkaline minerals to surface waters to elevate seawater alkalinity and enhance atmospheric CO_2 storage. Cement kiln dust (CKD) and lime kiln dust (LKD) are alkaline side streams from the cement and lime industry that

10 have OAE potential due to their widespread availability and fine particle size. Here, we evaluated the dissolution kinetics, CO_2 sequestration potential, and ecological risks of CKD and LKD by means of laboratory dissolution experiments. A reactive fraction (~25 % in LKD and ~29 % in CKD) dissolved rapidly within 24 hours, with most dissolution occurring within the first hour. Dissolution provided a concomitant alkalinity release that was higher for LKD (up to 8.0 ± 0.5 mmol alkalinity per g) than CKD (2.4 ± 0.2 mmol g^{-1}), thus providing a sizeable CO_2 sequestration capacity for LKD (297 ± 20 g CO_2 per g) and

15 CKD (88 ± 6 g CO_2 per g). Based on current industrial production rates, this translates into global CDR potentials of up to 8.7 ± 0.6 Mt CO_2 yr^{-1} for LKD and 25 ± 2 Mt CO_2 yr^{-1} for CKD, suggesting that both materials could serve as viable OAE feedstocks. Furthermore, we hypothesize that the substantial residual calcite content of LKD (~54 %) and CKD (~37 %) may provide additional sequestration via metabolic dissolution in marine sediments. However, kiln dust deployment will generate elevated turbidity levels that may exceed environmental thresholds, underscoring the need for carefully designed application

20 strategies to minimize local ecological impacts.

1 Introduction

As global temperatures continue to rise, the urgency for climate mitigation increases (IPCC, 2023). In addition to substantial cuts in greenhouse gas emissions, gigaton-scale atmospheric carbon dioxide removal (CDR) is needed to meet the goals of the Paris Agreement (Rockström et al., 2017; Minx et al., 2018; IPCC, 2023). One proposed CDR method is mineral-based ocean

25 alkalinity enhancement (OAE), which offers considerable removal potential and long-term CO_2 storage (Kheshgi, 1995; Renforth and Henderson, 2017). Mineral-based OAE targets the addition of specific basic minerals to the surface ocean, which

release alkalinity upon dissolution, thereby stimulating oceanic CO_2 uptake (Renforth and Henderson, 2017; Geerts et al., 2025).

A variety of minerals have been proposed as feedstock for mineral-based OAE, and approaches largely fall into two categories.

30 So-called "enhanced weathering" techniques target the addition of natural rock material containing silicates (e.g. olivine Mg_2SiO_4) or carbonates (e.g. calcite $CaCO_3$) to sediments, which then slowly dissolve up or in the seabed over a time scale of years to decades (Montserrat et al., 2017; Flipkens et al., 2023; Dale et al., 2024; Fuhr et al., 2025; Geerts et al., 2025). In contrast, "ocean liming" procedures involve the addition of industrially processed minerals such as slaked lime ($Ca(OH)_2$) or brucite $Mg(OH)_2$, thus targeting a much faster alkalinity release upon dissolution in the water column over a time scale of

35 minutes to hours (Renforth et al., 2013; Renforth and Henderson, 2017; Caserini et al., 2021; Foteinis et al., 2022; Kitidis et al., 2024). Slaked lime is produced by calcining limestone ($CaCO_3$) to form quicklime (CaO) (Eq. (1)), which is then hydrated (Eq. (2)) (Moras et al., 2022).

$$CaCO_3 \rightarrow CaO + CO_2 \tag{1}$$

$$CaO + H_2O \rightarrow Ca(OH)_2 \tag{2}$$

40 Upon dissolution in seawater, slaked lime releases alkalinity and binds CO_2 in the form of bicarbonate (HCO_3^-).

$$Ca(OH)_2 + 2CO_2 \rightarrow Ca^{2+} + 2HCO_3^- \tag{3}$$

Ocean liming has the benefit of rapid CO_2 sequestration upon deployment, and offers the potential to remove gigatons of atmospheric CO_2 annually, with ample global reserves to support deployment (Caserini et al., 2022; Foteinis et al., 2022). However, large-scale deployment would require a substantial increase in limestone mining and lime production, carrying

45 significant economic and environmental costs (Caserini et al., 2021; Foteinis et al., 2022). As a result, industrial by-products and mine tailings are attracting a growing interest for CDR applications, thanks to their lower processing costs, and alignment with circular economy principles (Bullock et al., 2021; Bullock et al., 2022; Moras et al., 2024).

The cement and lime industries are among the largest mineral production sectors globally, producing approximately 4.1 Gt of cement and 0.42 Gt of lime annually (CEMBUREAU, 2024; USGS, 2025). Both rely on the high-temperature calcination of

50 limestone in kilns to produce quicklime and cement clinker. This process generates fine particulate kiln dust, which is captured by air pollution control systems for recycling or disposal (Arulrajah et al., 2017; Barnat-Hunek et al., 2018). Kiln dust accounts

for 2–20 % of the kiln output, depending on process conditions and gas flow rates (Al-Refeai and Al-Karni, 1999; Elbaz et al., 2019; Al-Bakri et al., 2022; Ahmed et al., 2023). Lime kiln dust (LKD) mainly consists of unreacted limestone ($CaCO_3$) and calcium (hydr)oxides (CaO or $Ca(OH)_2$), while cement kiln dust (CKD) is a mix of unreacted feedstock, clinker dust, fuel ash,

55 halides, and other volatiles (Sreekrishnavilasam et al., 2006; Ban et al., 2022). Both types of kiln dust contain a substantial fraction of CaO, and $Ca(OH)_2$, which hence provides alkalinization potential upon addition to seawater (Eq. (3)).

Given their large-scale production, LKD and CKD hence show a potential as feedstocks for OAE, which is investigated and quantified here through laboratory experiments. OAE suitability was assessed by: (1) evaluating dissolution kinetics and alkalinity generation in seawater, and (2) monitoring changes in seawater properties during dissolution, specifically turbidity,

60 trace elements, and pH increases. These effects were compared to existing environmental guidelines to assess potential risks to marine ecosystems.

2 Material and methods

2.1 Solid phase characterization

The CKD and LKD were oven-dried at 40°C for 72 h before experimental use. Grain size distribution was determined with a

65 Malvern Mastersizer 3000 equipped with a Hydro LV dispersion system and operated at a stirring speed of 3000 RPM and no sonication prior to measurement. The dry solid phase density of the kiln dust was determined by measuring water displacement in a graduated cylinder (Dan-Asabe et al., 2013). To characterize the elemental composition, a 125 mg aliquot of dry, ball-milled (<2 μm) kiln dust was added to Teflon vessels and digested overnight at 90°C in a heat block with a mixture of 1.5 mL $HClO_4$, 1 mL HNO_3, and 2.5 mL HF. After cooling, the caps were removed, and the vessels were heated to 140°C to evaporate

70 HF, leaving a gel-like residue. Next, 25 mL of 4.5 % HNO_3 was added to each vessel, which was then capped and heated at 90°C for 2 hours. The resulting solutions were diluted and analyzed for elemental composition using ICP-OES (Avio 500, Perkin-Elmer) at the GeoLab (Utrecht University, The Netherlands). Quality control measures included a blank, two certified standards, and a duplicate sample. The mineralogical composition of the samples was determined in duplicate via quantitative X-ray diffraction (XRD) on a Bruker D8 Advance Eco diffractometer (Cu Kα, 40 kV, 25 mA) over 5–70° 2θ with 0.015° steps

75 and 0.5 s per step. Samples were rotated at 10 rpm using a 10 mm variable divergence slit, and patterns were recorded with a

LynxEye XE-T detector. Phase identification and quantification were performed using EVA and TOPAS (Bruker, V7). The

BET specific surface area was determined by N_2 adsorption using a Quantachrome NOVA 2200E at the laboratory for Process

Engineering for Sustainable Systems (KU Leuven, Belgium). The geometric specific surface area was calculated from the

grain size distribution results (Appendix A Sect. A1). Finally, the grain morphology and presence of secondary minerals on

80   kiln dust grains recovered from the dissolution experiments were analyzed via Scanning Electron Microscopy (SEM) using a

Phenom ProX SEM equipped with an energy dispersive spectrometer (EDS), operated at an accelerating voltage of 15 kV. For

SEM analysis, the dried kiln dust was mounted on aluminum (Al) pin stubs using double-sided carbon tape.

2.2 Dissolution experiments

The dissolution kinetics of LKD and CKD in seawater were assessed in two separate experiments (Table 1), hereafter referred

85   to as experiments I and II. In experiment I, the short-term dissolution behaviour was tracked via continuous pH monitoring.

Filtered (<0.2 µm) seawater from the Eastern Scheldt (saline water body in The Netherlands adjacent to the North Sea; salinity

32.3 ± 0.5) was obtained from Stichting Zeeschelp (Kamperland, The Netherlands). The filtered seawater (FSW) was aerated

for 24 hours before use to ensure atmospheric CO_2 equilibration. The initial seawater pH and total alkalinity (A_T) were analysed

(as described in Sect. 2.3). For A_T analysis, 55 mL seawater was collected in duplicate using a 60 mL plastic syringe, and

90   filtered (0.8/0.2 µm polyethersulfone (PES) membrane). Based on preliminary tests, three different masses of CKD and LKD

were added targeting a specific aragonite saturation state (Ω_{Arg}) at the end (final concentration and estimated Ω_{Arg} are provided

in Table 1). Experiment I was carried out in triplicate. Kiln dusts were weighed in small aluminium (Al) foil cups using a

micro balance (XP26 Excellence Plus, Mettler Toledo) and then transferred to 200 mL polystyrene vials with polyethylene

screw caps containing approximately 200 mL of FSW. Vials were weighed on an analytical balance (Sartorius TE3102S) to

95   precisely determine the mass of added seawater. Plastic vials were rinsed with 0.5 M HCl and ultrapure water (PURELAB®

flex 3, Elga Veolia) before usage. The pH electrode was inserted through a hole in the vial cap, which fit tightly to minimize

atmospheric CO_2 exchange. Vials were wrapped in tape to block light and contained minimal headspace. Subsequently, the

pH of the suspension was measured every minute over a period 8 hours (see pH measurement procedure below). Seawater

temperature was kept constant at 20°C during the incubation by means of a water bath (T100, Grant). Magnetic stirring was

100   applied at a rate of 700 rotation per minute (RPM) to ensure good mixing of the suspension. At the end of experiment I (after

~8 hours) , 55 mL of seawater was collected in duplicate for A_T analysis. Salinity was measured, and the samples were subsequently analysed for A_T (see Sect. 2.3).

To assess the alkalinity generation potential and the possibility of secondary mineral formation, we conducted a second, longer-term dissolution experiment. At the start of experiment II, clean 200 mL plastic vials were again filled with 200 mL of FSW on an analytical balance (TE3102S, Sartorius). Different amounts of LKD (11–111 mg kg^{-1}) and CKD (30–308 mg kg^{-1}) were added to achieve a target Ω_{Arg} ranging from 3.6 to 9.7 (Table 1). A control containing only 200 mL of FSW without kiln dust was also included. Vials were closed tightly and had minimal headspace to minimize gas exchange with the atmosphere. Experiment II was conducted at ambient room temperature (17.5–22.7 °C). Vials were subsequently placed on bottle rollers (ThermoFisher Scientific) at 14 RPM and incubated for either one or 15 days. The one-day incubation reflects the time needed for complete dissolution of the reactive phases in the kiln dusts, while the 15-day incubation allows for the verification of secondary mineral precipitation, in case this would occur. Samples for seawater A_T, dissolved inorganic carbon (DIC), turbidity, and dissolved metal analysis were collected in duplicate on both sampling days. Samples for A_T, DIC, and dissolved metals were filtered using 0.8/0.2 µm PES membrane filters. DIC samples (12 mL) were fixed with 10 µL of saturated $HgCl_2$ solution and stored at 4°C in 12 mL exetainers until analysis. Dissolved metal samples were acidified with TraceMetal™ Grade 67–69 % nitric acid to a final acid concentration of 1.4 % (v/v) and stored at -20°C prior until analysis. The remaining suspension in the incubation vials was filtered through a 0.2 µm polycarbonate membrane filter to collect solids, which were rinsed with deionized water and then oven dried at 40°C in preparation for SEM-EDX analysis.

Table 1. Experimental specifications of the two dissolution experiments (I and II). Target aragonite saturation state (Ω_{Arg}), concentrations of lime kiln dust (LKD), cement kiln dust (CKD), incubation time and temperature, and seawater stirring method are provided.

Exp.	Target Ω_{Arg}	LKD concentration (mg kg^{-1})	CKD concentration (mg kg^{-1})	Incubation time (days)	Temperature (°C)	Stirring method
I	3.6	10.9	29.9	0.33	20	Magnetic (700 RPM)
	5.7	47.7	130.3			

	9.7	113.07	309.2			
II	3.6	10.75	30.12	1 or 15	17.5–22.7	Rotation (14 RPM)
	4.2	20.96	47.93			
	5.2	37.15	88.85			
	5.7	46.49	129.12			
	7	69.12	191.81			
	8.4	90.94	253.35			
	9.7	110.70	307.84			

2.3 Seawater physicochemical analyses

Seawater salinity and pH were measured with an Orion™ DuraProbe™ 4-Cell conductivity probe (Thermo Scientific) and Unitrode pH electrode (Metrohm) connected to an Orion Star A215 pH/conductivity meter. The pH electrode was calibrated

125   using 35 salinity TRIS (2-amino-2-hydroxy-1,3-propanediol) and AMP (2-aminopyridine) buffers, and the pH was calculated on the total hydrogen ion scale following Dickson et al. (2007).

For A_T analysis, samples were titrated with 0.1 M HCl using an automated titrator setup (888 Titrando with 814 USB Sample Processor, Metrohm). The titrant was calibrated with certified reference material (batch 209; OCADS). A_T was derived from the titrant volume and electromotive force measurements recorded by the Unitrode pH electrode, using a non-linear least-

130   squares method as described by Dickson et al. (2007). Blank FSW samples were analyzed at the start of the run, after every tenth sample, and at the end for quality control, yielding relative standard deviations (RSD) smaller than 1.1 %. The specific A_T release $\Delta N_{AT}(t)$ at a given incubation time t, and expressed in mmol A_T per g of kiln dust, was derived via

$$\Delta N_{AT}(t) = (A_T(t) - A_T(t_0)) \frac{m_{FSW}}{m_{KD}} \tag{4}$$

Here, $A_T(t)$ represents the seawater alkalinity (mmol kg^{-1}) at a given incubation time, $A_T(t_0)$ is the alkalinity (mmol kg^{-1}) of

135　the blank FSW at the start of the experiment, m_{FSW} is the mass of FSW added to the incubation vials (kg), and m_{KD} is the

mass of added kiln dust (g).

In experiment I, the A_T was only measured at the begin and end of the experiment, and so only one $\Delta N_{AT}(t)$ value can be

calculated. To verify the observed alkalinity release, we calculated a theoretical value based on measured pH. To this end, the

initial DIC of the seawater was first calculated from measured values of pH, A_T, temperature, and salinity using the AquaEnv

140　package in R with default settings (Hofmann et al., 2010). Under the assumption that DIC remained constant throughout the

experiment, the corresponding A_T was then calculated from the measured pH and fixed DIC. The difference between this

calculated A_T and the starting A_T was used to compute $\Delta N_{AT}(t)$, and the value at the end (8 hours) was compared to the

measured $\Delta N_{AT}(t)$.

For experiment I, the fraction of reactive phases in the kiln dust that dissolved over time, $\chi_{diss}(t)$ (%), was determined by

145　normalizing $\Delta N_{AT}(t)$ to the maximum experimentally observed specific A_T increase ($\Delta N_{AT,max}$):

$$\chi_{diss}(t) = \frac{\Delta N_{AT}(t)}{\Delta N_{AT,max}} 100 \tag{5}$$

Seawater DIC concentrations were measured using a DIC analyzer (AS-C6L, Apollo SciTech) coupled to a trace gas analyzer

(LI-7815, LI-COR). Measurements were repeated until the relative standard deviation (RSD) for at least three repeats was ≤0.1

%. DIC concentrations were determined using a calibration curve based on an internal standard solution (0.002 M NaHCO$_3$)

150　adjusted to a salinity of 30 ppt with NaCl and spiked with 0.05 % (v/v) saturated HgCl$_2$. This internal standard was calibrated

against certified reference material (CRM; batch 209, OCADS). For quality control, CRM (batch 209, OCADS) was analyzed

at the start and end of the sequence, and the internal standard was run at the start and after every eight samples. Quality control

checks consistently yielded an RSD ≤0.25 %.

The remaining seawater carbonate chemistry parameters, including the aragonite and calcite saturation state and seawater pH

155　on a total scale, were calculated using the AquaEnv package in R (Hofmann et al., 2010). Measured A_T, DIC, salinity, and

temperature were given as input values, with all other parameters set to their default values.

Seawater samples for dissolved trace metal analysis were thawed and diluted 20-fold with 2 % (v/v) TraceSELECT™ HNO$_3$

(Honeywell Fluka) to a final volume of 10 mL. Before analysis, samples were spiked with 100 µL of an internal standard

solution (10 ppm Y; Alfa Aesar) and analyzed using high-resolution inductively coupled plasma mass spectrometry (HR-ICP-

160 MS; Agilent 7850) at the ELCAT group, University of Antwerp, Belgium.

Seawater turbidity was measured with a HI98713 ISO portable turbidity meter (Hanna Instruments) which was calibrated with

four turbidity standards (<0.1, 15, 100, and 750 FNU, Hanna Instruments) before each use.

2.4 Saturation state calculations

Saturation state (Ω) values for kiln dust mineral phases were calculated using PHREEQC Interactive (version 3.7.3-15968)

165 with the LLNL thermodynamic database (Parkhurst and Appelo, 2013). Input parameters included measured seawater

temperature, salinity, A_T, and pH. Major constituent concentrations (Cl, Na, Mg, K, Ca, SO_4) were derived based on the

average composition of natural seawater, scaled to measured salinity (Hem, 1985). Aragonite and calcite saturation states were

not computed in PHREEQC but were instead calculated using the AquaEnv package in R, as described previously (Hofmann

et al., 2010).

170 2.5 Statistical analyses

Differences in seawater physico-chemistry across kiln dust concentrations and incubation times were assessed using two-way

analysis of variance (ANOVA). The best fitting models were determined by the ANOVA and the lowest Akaike Information

Criterion (AIC). Normality and homoscedasticity of residuals were evaluated both visually (via QQ and residual plots) and

statistically (via Shapiro-Wilk and Levene's tests). Post-hoc pairwise comparisons were performed using estimated marginal

175 means (EMMs) with Holm-adjusted p-values. Comparisons were conducted within each concentration, adjusting for

incubation time, and vice versa. Data are presented as mean ± standard deviation (S.D.), unless otherwise specified. All

statistical analyses were performed in RStudio (version 2024.12.0+467) using R version 4.3.3 (R Core Team, 2022).

3   Results

3.1   Kiln dust physicochemical properties

180   XRD analysis revealed that the kiln dusts contained substantial amounts of calcite ($CaCO_3$; CKD ~37 % and LKD ~54 %; Table 2) and amorphous phases (~34 % in CKD and ~14 % in LKD). Furthermore, lime (CaO), portlandite ($Ca(OH)_2$), quartz (SiO_2) and anhydrite ($CaSO_4$) were additionally present in both kiln dusts at concentrations of 0.1–20 %. Finally, CKD also contained 0.9 % sylvite (KCl), 9.5 % syngenite ($K_2Ca(SO_4)_2.H_2O$), and 3.9 % Aphthitalite ($(K,Na)_3Na(SO_4)_2$) (Table 2). Both materials exhibited a relatively wide grain size distribution (Table 2 and Appendix A Fig. A1), but CKD (D50 = 8.4 ± 0.1 µm)

185   was significantly finer than LKD (D50 = 72 ± 4 µm). The observed elemental composition was congruent with the XRD results, showing high calcium contents in both CKD (27.8 wt%) and LKD (44.9 wt%), which fall within the range previously reported for CKD (14–46 %) and LKD (20–49 wt%) (Collins and Emery, 1983; Pavía and Regan, 2010; Latif et al., 2015; Drapanauskaite et al., 2021; Dvorkin and Zhitkovsky, 2023). While LKD exhibited relatively low levels of trace elements, CKD showed elevated concentrations, particularly of Zn (0.65 wt%) and Pb (0.15 wt%) (Table 2). Further details on the

190   elemental composition are provided in Appendix A Table A1.

Based on the mineralogical composition, the theoretical alkalinity release upon dissolution in seawater was calculated from the reaction stoichiometry. Saturation state analysis (Appendix B Fig. B2) show that seawater is undersaturated ($\Omega < 1$) with respect to most mineral phases present in the kiln dusts, with the exception of calcite and quartz. This indicates that dissolution is thermodynamically favourable, although it may be limited by kinetic constraints. Among the undersaturated minerals,

195   anhydrite, sylvite, aphthitalite, and syngenite do not contribute to alkalinity upon dissolution in seawater. In contrast, dissolution of portlandite and lime each generates 2 moles of A_T per mole (Eq. (3)), corresponding to maximum alkalinity contributions of 8.8 mmol g^{-1} for LKD and 1.3 mmol g^{-1} for CKD, respectively.

Table 2. Physicochemical properties of the experimental cement kiln dust (CKD) and lime kiln dust (LKD). ND indicates that the phases were not detectable. The complete measured elemental composition is provided in Appendix A Table A1.

Mineral composition (% w/w)	CKD	LKD
Calcite ($CaCO_3$)	37.0	53.8
Lime (CaO)	1.5	9.4

Portlandite ($Ca(OH)_2$)	2.8	20.1
Quartz (SiO_2)	3.4	0.13
Anhydrite ($CaSO_4$)	4.7	2.2
Sylvite (KCl)	0.9	ND
Syngenite ($K_2Ca(SO_4)_2 \cdot H_2O$)	9.5	ND
Aphthitalite ($(K,Na)_3Na(SO_4)_2$)	3.9	ND
Amorphous phases	34.3	14.4
Theoretical alkalinization potential (mmol g^{-1})	1.5	8.8
Textural composition		
D10 (µm)	2.2 ± 0.02	6.4 ± 0.2
D25 (µm)	3.9 ± 0.02	22 ± 1
D50 (µm)	8.4 ± 0.05	72 ± 4
D75 (µm)	24 ± 0.3	172 ± 12
D90 (µm)	49 ± 0.9	327 ± 35
Geometric specific surface area (m² g^{-1})	0.455 ± 0.007	0.121 ± 0.004
BET specific surface area (m² g^{-1})	4.2	3.2
Particle density (g cm^{-3})	2.71 ± 0.18	2.87 ± 0.14
Elemental composition (% w/w)		
Ca	27.8	44.9
Mg	0.56	0.22
Zn	0.65	0.0029
Pb	0.15	<0.000014

200

3.2 Kiln dust dissolution speed

The dissolution kinetics of CKD and LKD in seawater (salinity 32 ± 0.1, temperature 20°C, initial pH of 8.05 ± 0.03) were
investigated in experiment I over a period of 8 hours at three different kiln dust concentrations under continuous stirring. A
rapid increase in seawater pH was observed for both kiln dusts: about 69 ± 8 % of the total pH rise occurred within the first
205 ~10 minutes, after which the pH continued to slowly increase for the rest of the 8-hour incubation (Fig. 1A). The final pH

10

increase $\Delta pH = pH(t_{end}) - pH(t_0)$ was greater for LKD than for CKD and increased with higher kiln dust concentrations (Fig. 1C).

Upon dissolution, the percentage of reactive phases that had effectively dissolved $\chi_{diss}(t)$ rapidly increased with time, with 50 % of the reactive phases dissolved within 9.5 ± 3 minutes for LKD and within 9.9 ± 2.4 minutes for CKD (Fig. 1B). At the

210   lowest kiln dust concentration, approximately 83 ± 9 % of the reactive phases in LKD and 72 ± 12 % in CKD had dissolved after one hour, which increased to 88 ± 7 % and 82 ± 17 % respectively after 8 hours. At higher kiln dust concentrations, the percentage of dissolved reactive phases was generally lower (Fig. 1B). This effect is likely caused by secondary mineral precipitation, and not so much by reduced dissolution, as further discussed in Sect. 3.3.

Kiln dust dissolution in seawater resulted in a concomitant increase in alkalinity, $\Delta A_T = A_T(t) - A_T(t_0)$, which increased with

215   higher kiln dust concentrations (Fig. 1D), and attained values ranging from 60 to 447 µmol kg^{-1} for CKD and 110 to 416 µmol kg^{-1} for LKD, depending on the applied kiln dust concentration. Notably, the relationship between ΔA_T and kiln dust addition was non-linear and showed a saturating effect (Fig. 1D), suggesting a decreased specific alkalinity release at higher kiln dust concentrations.
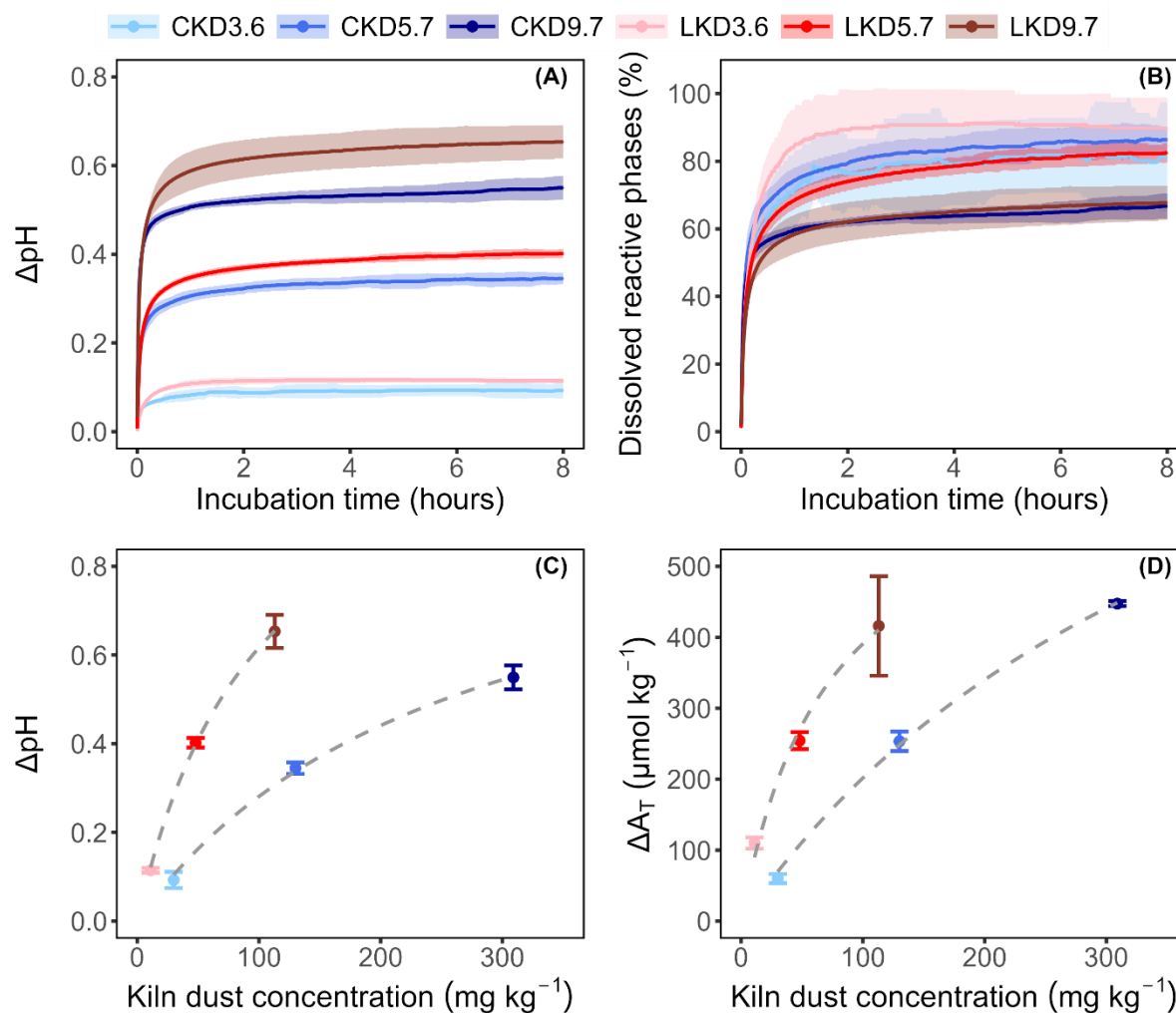
Figure 1. Results (Mean ± S.D., N =3) obtained in experiment I for three concentrations of cement kiln dust (CKD, in blue) and lime kiln dust (LKD, in red). (A) Change in seawater pH (ΔpH) as a function of incubation time. pH on total scale. (B) Estimated percentage of reactive kiln dust phases (χ_{diss}) dissolved as a function of incubation time. Change in (C) seawater pH and (D) total alkalinity (ΔA$_T$) after 8 hours as a function of kiln dust concentration. Fitted non-linear least squares curves are shown as a grey dashed line in (C) and (D).

3.3 Alkalinity generation

In experiment II, we investigated the alkalinity release from LKD and CKD after 1 and 15 days of incubation across a range of kiln dust concentrations. Dissolution resulted in a change in seawater pH and A$_T$ that markedly varied with kiln dust concentration (Fig. 2A and 2B). After one day, the pH increased showed a non-linear (saturating) increase with the kiln dust concentrations for both LKD and CKD (Fig. 2A), consistent with the results of experiment I after 8 hours (Fig. 1C). Yet after

15 days of incubation, the ΔpH curve showed a marked difference between LKD and CKD. For CKD, the ΔpH curve at 15 days showed a similar saturating shape as after 1 day, though with slightly decreased ΔpH values at higher kiln dust concentrations (suggesting a process at play that reduced pH). For LKD, the ΔpH curve at 15 days was entirely different compared to day 1, with a marked decrease in ΔpH at higher concentrations. For the highest LKD concentration examined

235   (111 mg kg^{-1}), the pH after 15 days was almost the same as at the start (ΔpH = 0.17 $\pm$ 0.14) (Fig. 2A).

The observed changes in alkalinity (Fig. 2B) were congruent with those seen for ΔpH. After one day, ΔA_T showed a monotonous increase with the CKD concentration, while for LKD, the ΔA_T curve showed a maximum at higher concentrations (Fig. 2B). The ΔA_T curves for LKD and CKD obtained at 15 days of incubation were markedly different from those at day 1, showing reduced ΔA_T values at higher kiln dust concentrations, indicative of a process that consumes alkalinity. Notable, for

240   LKD, ΔA_T became negative at higher concentrations (Fig. 2B), indicating a removal of alkalinity compared to the initial situation.

The specific alkalinity release quantifies the alkalinity release per mass of kiln dust added, and generally decreased for higher concentrations (Fig. 2C). The highest values for the specific alkalinity release were obtained at the lowest kiln dust concentrations applied (21 mg kg^{-1} and lower for LKD, 89 mg kg^{-1} or lower for CKD). The maximum specific alkalinity

245   release for LKD (8.02 $\pm$ 0.53 mmol g^{-1}) was more than three times higher than that of CKD (2.38 $\pm$ 0.16 mmol g^{-1}), and generally agreed with the theoretically calculated value (8.8 mmol g^{-1} for LKD and 1.3 mmol g^{-1}; see Sect. 3.1). The specific alkalinity release after 15 days showed a clear difference with day 1, which was more pronounced for LKD compared to CKD. At the low application concentrations, the specific A_T release after 15 days of incubation was not statistically significantly different from the release after 1 day (Fig. 2C), thus indicating that all A_T-generating reactive phases had dissolved within the

250   first day and no alkalinity removal took place. Yet, the specific A_T release decreased substantially at higher kiln dust concentrations, with a more pronounced decline for LKD compared to CKD. In the case of LKD, the specific A_T release became even negative after 15 days of incubation, thus indicating overall alkalinity consumption rather than production (Fig. 2C).

To verify whether secondary carbonate precipitation could be responsible for the observed alkalinity consumption, we

255   calculated the seawater aragonite saturation state (Ω_{Arg}). The increase in seawater total alkalinity (A_T) from kiln dust dissolution

led to a corresponding rise in aragonite saturation state (Ω_{Arg}) from an initial value of 3.0 ± 0.1 at the start of the experiment II

to 9.3 ± 0.3 and 10.3 ± 0.1 after 1 day of incubation at the highest concentrations of LKD and CKD, respectively (Fig. 2D).

Moreover, a significant decrease in Ω_{Arg} was observed at day 15 compared to day 1 for LKD concentrations above 21 mg kg⁻¹

and for CKD concentrations above 89 mg kg⁻¹, suggesting alkalinity scavenging by secondary mineral precipitation. This

260 decrease became more pronounced at higher application concentrations and was notably greater for LKD compared to CKD.

For the highest LKD concentration investigated (111 mg kg⁻¹), Ω_{Arg} after 15 days (2.5 ± 0.6) was not significantly different

from the initial Ω_{Arg} value (Fig. 2D).
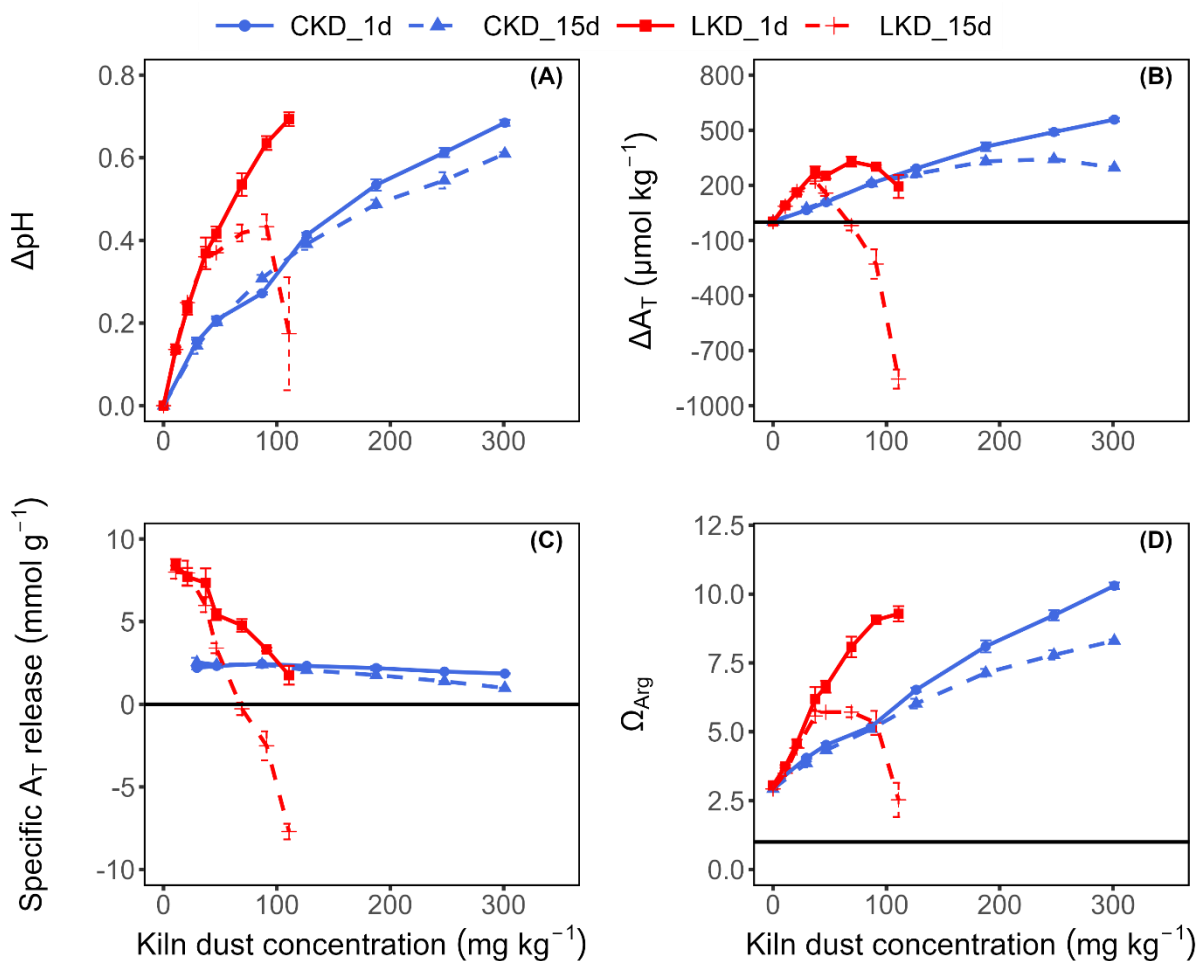
Figure 2. Results obtained in experiment II for different concentrations of cement kiln dust (CKD, blue) and lime kiln dust (LKD,
265 **red). (A) Change in seawater pH (ΔpH), (B) total alkalinity (ΔA$_T$, expressed in μmol kg⁻¹), (C) Specific A$_T$ release (mmol mg⁻¹) and**
(D) aragonite saturation state (Ω$_{Arg}$) as a function of the kiln dust application concentration (mg kg⁻¹). Results (as mean ± S.D., N=3)
after 1 day (solid lines) and 15 days of incubation (dashed lines) are shown.

3.4 Mineral morphology and secondary mineral precipitation

The morphology of kiln dust particles was compared before and after chemical weathering (i.e., fresh material versus samples

270   retrieved after 15 days in experiment II). Fresh lime kiln dust (LKD) consisted of a heterogeneous mixture of particles of varying size and shape, dominated by small (<10 µm), irregular, calcium-rich particles (~10–20 at%) (Fig. 3A). In weathered LKD, the abundance of these fine particles decreased (Fig. 3C, E), while larger particles developed rough surface texture (representative particle indicated by red arrow in Fig. 3C), suggesting dissolution of surface phases. After 15 days of incubation at the highest LKD concentration, most particles were extensively coated with bundles of needle-like, calcium-rich precipitates

275   (Fig. 3E).

Fresh cement kiln dust (CKD) also contained irregularly shaped particles of various sizes (Fig. 3B). In addition, spherical fly ash particles of varying diameters were prominent in both fresh and weathered CKD samples and showed no signs of weathering during experiment II (red arrows in Fig. 3B, D, F). In contrast to LKD, weathered CKD particles showed neither roughened surfaces nor secondary calcium carbonate precipitation, regardless of concentration or incubation duration (Fig.

280   3D, F).
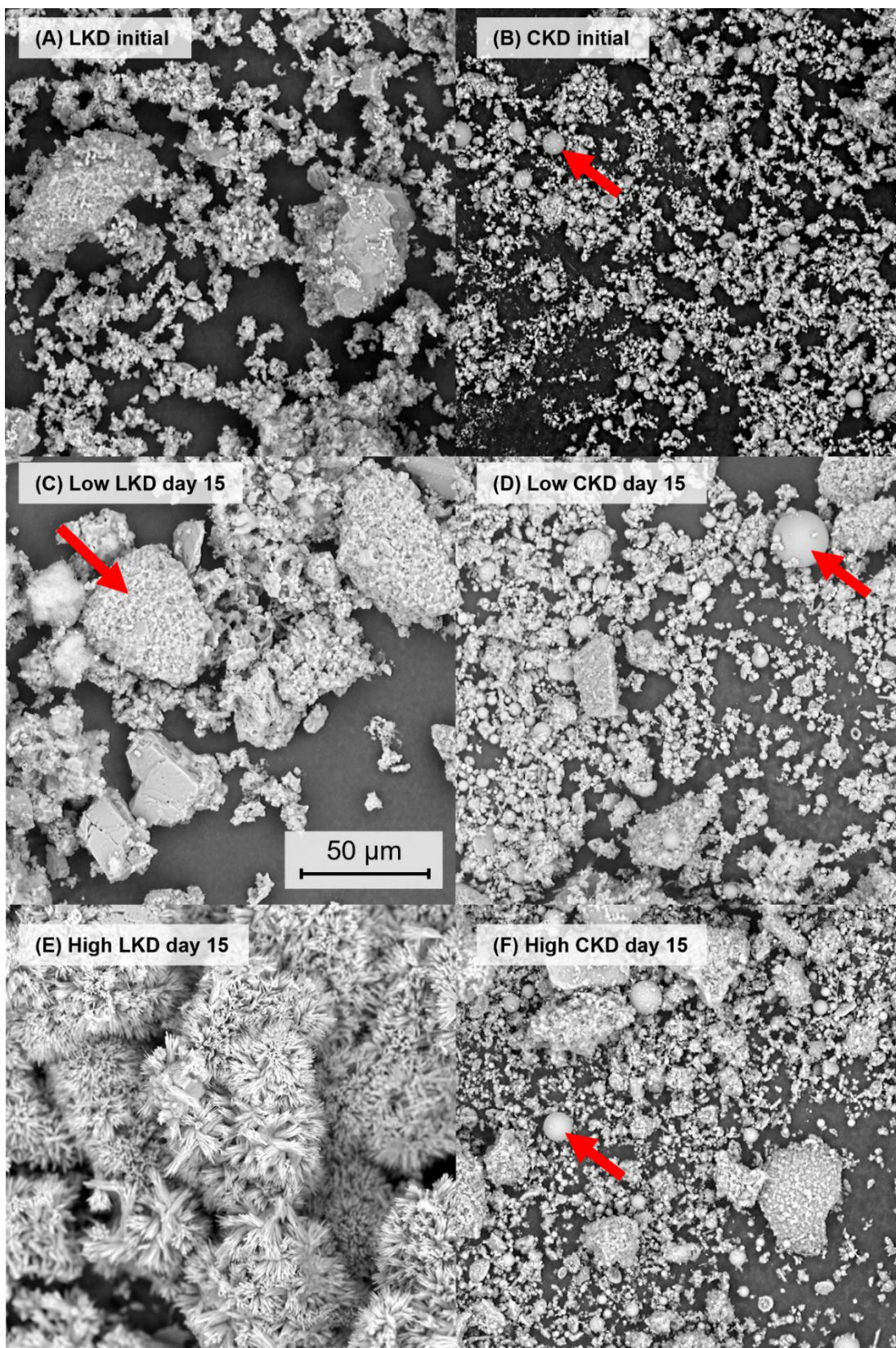
Figure 3: Representative Scanning electron microscopy (SEM) images of kiln dust particles at different time points in experiment II. (A) Fresh lime kiln dust (LKD) and (B) fresh cement kiln dust (CKD). Images (C) and (D) show CKD and LKD particles after 15 days of incubation at low application concentrations (88.85 mg kg⁻¹ and 20.96 mg kg⁻¹, respectively). Images (E) and (F) show CKD and LKD particles incubated for 15 days at the highest application concentrations (307.84 mg kg⁻¹ and 110.7 mg kg⁻¹, respectively). Red arrows in panels (B), (D), and (F) mark fly ash particles, while the red arrow in panel (C) highlights the rough surface texture of a weathered large LKD particle.

3.5 Turbidity and trace metals

The turbidity in solution after 1 and 15 days increased linearly with the applied kiln dust concentration, as expected. At equivalent application concentrations, turbidity was ~2.4 times higher for CKD than for LKD, consistent with the finer grain size of the CKD (Fig. 4A). After 15 days of incubation, seawater turbidity rose from 0.33 ± 0.10 FNU in the initial filtered seawater to 281 ± 3 FNU at the highest CKD concentration and 52 ± 3 FNU at the highest LKD concentration. Turbidity was slightly but significantly greater on day 15 compared to day 1 at higher kiln dust concentrations (>253 mg kg⁻¹ for CKD; >69 mg kg⁻¹ LKD), possibly due to fragmentation of unreacted kiln dust particles and/or the formation of secondary calcium carbonate providing fine particles in solution (Fig. 4A).

The accumulation of dissolved Fe, Ni, Cu, Zn, As, and Pb was low in both the LKD and CKD incubations and showed no clear dependence on kiln dust concentration (Appendix B Fig. B3). So trace metal release was limited, apart from vanadium (V) in the CKD incubation, which linearly scaled with the kiln dust concentration (Fig. 4B). After 15 days, V accumulation reached 0.51 ± 0.09 µmol kg⁻¹ at the highest CKD concentration and 0.008 ± 0.001 µmol kg⁻¹ at the highest LKD concentration, respectively. These values agreed relatively well with the expected accumulations of 0.63 µmol kg⁻¹ and 0.0033 µmol kg⁻¹, based on the elemental composition and assuming that V belongs to the dissolvable fraction of the kiln dusts (Appendix B Fig. B4). The dissolved V accumulation after 15 days did not differ significantly from that on day 1, suggesting that V is not involved in secondary reactions. For CKD, concentration-dependent accumulation of Al, Cr, and Mn was also observed, though the accumulation represented only a small fraction of what was expected based on complete dissolution of reactive phases: 2–11 % for Al, 24–35 % for Cr, and 0.6–2 % for Mn (Appendix B Fig. B3-4).
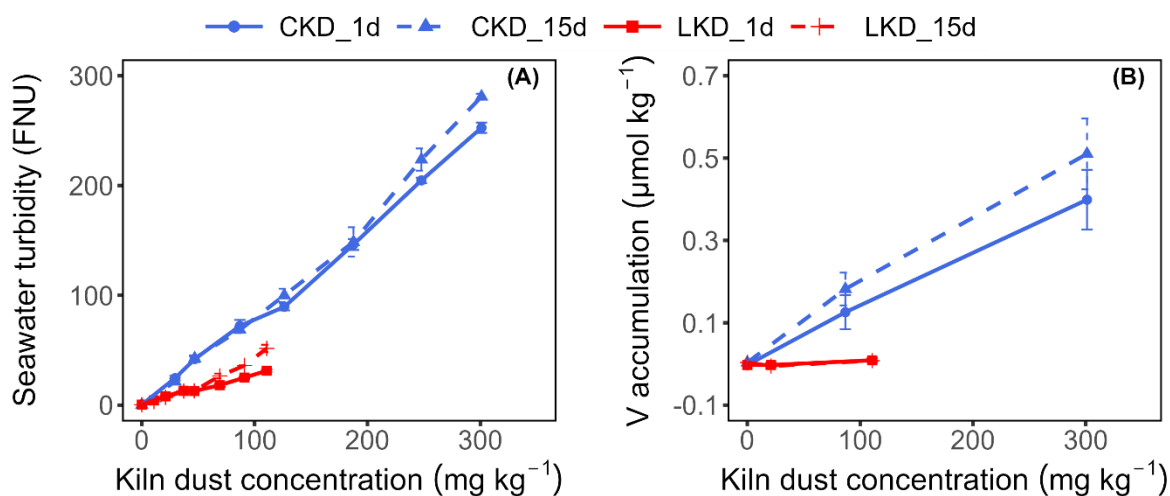
Figure 4. Impact of dissolution on turbidity and trace metals in experiment II. Results (as mean ± S.D., N=3) are shown for lime kiln dust (LKD, red) and cement kiln dust (CKD, blue) after 1 day (solid lines) or 15 days (dashed lines) of incubation. (A) Seawater
310 **turbidity (FNU) and (B) accumulation of dissolved vanadium (V, µmol kg^{-1}) as a function of the kiln dust concentration.**

4 Discussion

4.1 Dissolution kinetics and alkalinity generation potential

The dissolution kinetics of LKD and CKD were studied in natural seawater (salinity: 32.3 ± 0.5; temperature: 17.5–22.7 °C) under continuous stirring. LKD mainly consists of calcite ($CaCO_3$), with smaller amounts of quartz, portlandite, lime,

315 anhydrite, mullite, and dolomite (Strydom et al., 1996; Ban et al., 2022). CKD is more compositionally complex, typically containing calcite along with various sulfates, chlorides, silicates, and aluminates, including belite, aphthitalite, spurite, and ferrite (Ayman et al., 2004; Siddique and Rajor, 2012; Beltagui et al., 2017; Lee and Choi, 2024; Nikolov et al., 2025). The compositional complexity of kiln dusts underscores the need for detailed mineralogical and chemical characterization to properly assess the CDR potential and environmental risks in OAE applications.

320 Both materials generated significant alkalinity upon dissolution in seawater, with maximum values of 8.02 ± 0.53 µmol mg^{-1} for LKD and 2.38 ± 0.16 µmol mg^{-1} for CKD after 24 hours. This alkalinity originated from a fraction of reactive phases contained within the kiln dust (25 % by mass in LKD; 29 % in CKD), which we estimated based on the mineral components that are unstable in seawater. Consequently, both LKD and CKD contained a substantial amount of unreactive phases that

18

remained inert over the 15-day duration of our short-term experiments. In preliminary tests, replacement of the overlying

325   seawater after 15 days did not result in further dissolution or alkalinization. The residual fraction in LKD and CKD consisted

primarily of calcite, which is supersaturated in surface seawater (Appendix B Fig. B2G), preventing its dissolution (Sulpis et

al., 2021).

The experimentally observed alkalinity release from LKD (8.02 ± 0.53 mmol g^{-1}) was slightly lower than the theoretical value

(8.8 mmol g^{-1}), whereas CKD released substantially more alkalinity (2.38 ± 0.16 mmol g^{-1}) than predicted from its

330   mineralogical composition (1.3 mmol g^{-1}). In LKD, alkalinity release was fully be attributed to the dissolution of portlandite

($Ca(OH)_2$) and lime (CaO), whereas in CKD these phases explained only about half (54 ± 3 %) of the release. The remaining

alkalinity release from CKD likely originated from dissolution of amorphous phases, including (partially dehydrated) clay

minerals, reactive amorphous silica, and kiln-derived materials such as fly ash or slag (Khanna, 2010; Pavía and Regan, 2010).

There is a possibility that some reactive phases remained sequestered in larger particles and did not react with seawater on the

335   time scale of the experiment. However, this fraction is likely minor, since the experimentally observed alkalinity release was

close to, or even exceeded, the maximum theoretically predicted values from the mineralogical composition.

The dissolution of kiln dusts was rapid, with 65–92 % of the reactive phases dissolving within the first hour of incubation (Fig.

1B). This estimate assumes a constant DIC concentration over time, although values could have increased due to CO_2 uptake

from the (limited) vial headspace or decreased through secondary aragonite precipitation at higher application concentrations.

340   Therefore, the χ_{diss} values reported (Fig. 1B) should be considered best estimates based on available data. Nonetheless, the

rapid alkalinity release highlights the potential of kiln dusts for OAE. Using our measured particle size distribution and

assuming particle sinking follows Stokes' law, all CKD particles and most LKD particles (85 ± 2 % V/V) will remain in the

surface ocean mixed layer (assumed to be 200 m) for about one hour, allowing sufficient time for most reactive phases to

dissolve and generate alkalinity (Appendix A Sect. A2). However, ocean turbulence and particle aggregation induced by

345   biological exudates can significantly accelerate particle sinking (Yang and Timmermans, 2024). Hence, application areas need

to be carefully chosen to ensure that dissolution of the reactive phase takes place in the ocean mixed layer.

4.2 Emergence and prohibition of secondary precipitation

Alkalinity addition to seawater should avoid triggering secondary precipitation reactions that consume alkalinity, as these reduce the overall efficiency of OAE. Specific A_T release significantly decreased at concentrations above 21 mg kg⁻¹ for LKD

350 and 89 mg kg⁻¹ for CKD, with greater reductions at higher kiln dust concentrations and longer incubation times (Fig. 2C). Furthermore, the decrease was stronger for LKD relative to CKD at equivalent aragonite saturation states (Fig. 2C and 2D). The observed reduction in specific A_T release can be attributed to secondary mineral precipitation, as indicated by the reduction in seawater DIC concentrations (Appendix B Fig. B1) and the formation of Ca-rich needle-like structures on weathered LKD grains (Fig. 3E). These needles resemble the early developmental stage of aragonite precipitates, as described by Suitner et al.

355 (2024). No significant A_T loss occurred at Ω_{Arg} values of 5.1 ± 0.07 for CKD and 4.5 ± 0.1 for LKD, but significant loss was observed at higher kiln dust concentrations. This aligns with the previously documented $\Omega_{Arg} = 5$ threshold for secondary aragonite precipitation, when fine-grained (<63 µm) quick lime (CaO) or slaked lime (Ca(OH)$_2$) powder from a chemical and industrial supplier are added to natural seawater at 35 salinity (Moras et al., 2022). While the Ω_{Arg} precipitation threshold was similar for LKD and CKD, the CKD treatment showed a lower precipitation rate, possibly because CKD has a lower content

360 of Ca-rich phases (e.g., calcite, lime and portlandite), which can serve as nucleation sites for aragonite precipitation (Pan et al., 2021; Moras et al., 2022; Suitner et al., 2024). Prolonged exceedance of critical saturation thresholds can trigger "runaway CaCO$_3$ precipitation", leading to a net A_T loss, as seen at the highest LKD concentration after 15 days (Fig. 2A) (Moras et al., 2022). Based on our temporal dissolution data (Fig. 1A-B), it is recommended to adjust the OAE dispensing and deployment procedure in such a way, that dilution to $\Omega_{Arg} < 5$ occurs within minutes as to minimize secondary mineral precipitation.

365 ## 4.3 Potential ecological impacts of kiln dust dissolution

Mineral-based OAE shows promise as a CDR technique, but its effects on seawater carbonate chemistry, turbidity, and trace element concentrations could lead to adverse ecological impacts that need to be mitigated (Bach et al., 2019; Flipkens et al., 2021). For ocean liming, rapid mineral dissolution can cause acute spikes in pH and alkalinity right after discharge, raising potential environmental concerns (Caserini et al., 2021; Varliero et al., 2024). In our study, CKD and LKD caused fast,

370 concentration-dependent seawater pH increases (Fig. 1A). Model predictions indicate that pH could rise by 1 to 1.5 units for

several minutes during ship-based ocean liming Caserini et al. (2021), which may have an impact on marine life if pH exceeds 9 (ANZECC and ARMCANZ, 2000; Pedersen and Hansen, 2003; Camatti et al., 2024). To avoid temporary exceedances of pH 9, CKD concentrations should stay below 343–502 mg kg^{-1}, and LKD below 102–149 mg kg^{-1}, depending on local seawater conditions (A_T = 2350 µmol kg^{-1}, DIC = 2100 µmol kg^{-1}, salinity = 35, temperature = 10–25 °C).

375 Seawater turbidity rose linearly with kiln dust concentration and was greater for CKD than LKD at equivalent doses, consistent with the finer grain size of CKD (Fig. 4A). Increased turbidity could reduce primary production by obstructing light (Cloern, 1987; Köhler et al., 2013), and impair feeding efficiency in marine suspension feeders (e.g. bivalves, sponges, and tunicates) (Cheung and Shin, 2005; Bell et al., 2015) and visual foragers (e.g. most marine fish and mammals) (Lowe et al., 2015; Lunt and Smee, 2020). Additionally, the sinking rate of organic carbon to the deep sea could be enhanced by the adsorption of 380 organic molecules onto suspended particles (Santinelli et al., 2024), which may affect ecosystem carbon cycling, but also would provide additional CDR. Turbidity guidelines are designed to protect marine life from harmful increases: for example, in Canada, seawater turbidity should not increase by more than 8 NTU over 24 hours in clear water, or 5 NTU at any time in already turbid water (8–50 NTU background) (Singleton, 2021). To stay within these limits, ambient CKD concentrations must remain below 9.7 mg kg^{-1} in clear water and 6.1 mg kg^{-1} in turbid water, while LKD concentrations should stay below 385 23.7 and 14.8 mg kg^{-1}, respectively (Fig. 4B). In real applications, kiln dust will be rapidly mixed into much larger volumes of surface water, meaning that the allowable concentration in the input stream will depend on the discharge rate and the intensity of local turbulence.

At the turbidity thresholds, the maximum seawater alkalinity enhancement would range from 119 to 190 µmol A_T kg^{-1} for LKD, and only 15 to 23 µmol A_T kg^{-1} for CKD. The corresponding increases in pH (assuming A_T = 2350 µmol kg^{-1}, pCO$_2$ = 390 420 µatm, salinity = 35, and temperature = 10–25 °C) are ΔpH = 0.18–0.30 for LKD and ΔpH = 0.002–0.004 for CKD, both remaining well below the threshold of ΔpH = ~0.9 (rise up to pH 9). Moreover, the carrying capacity of natural coastal and shelf ecosystems appears to be large enough to execute LKD- and CKD-based OAE within the existing turbidity constraints. For example, the North Sea has a total volume 54.000 km^3 and an average residence time of ~1 year (Lee, 1980; Liu et al., 2019). A hypothetical one-time application of LKD-based OAE across the entire North Sea at the maximum level of 119 µmol

395 A_T kg^{-1} for LKD, would require 823 Mton of LKD, which is ~28 times larger than the global annual LKD production rate

(~29 Mton yr^{-1}).

The dissolution of alkaline minerals can release trace metals into the environment, which may be beneficial or toxic to marine

life (Bach et al., 2019; Flipkens et al., 2021). CKD contained notable amounts of Zn and Pb, while LKD had generally low

trace element levels (Appendix A Table A1). Trace metal content in kiln dusts varies with raw materials, fuels, and kiln

400 operations, and is typically higher and more variable in CKD (Siddique and Rajor, 2012; Nyström et al., 2019). In experiment

II, metal release from LKD was limited, whereas CKD showed concentration-dependent release of V, Cr, Mn, and Fe (Fig.

4B; Appendix B Fig. B3). Regulatory guidelines exist to protect aquatic life from trace metal toxicity. For example, Tulcan et

al. (2021), proposed a seawater V guideline of 0.022 µmol L^{-1}, which would require CKD concentrations to remain below

14.1 mg kg^{-1} to avoid exceedance. Higher application rates may be permissible under other guidelines for V, Cr, or Mn.

405 Residual kiln dust mixing with surface sediments may elevate metal levels, particularly Zn and Pb from CKD. Sediment

Quality Guidelines (SQGs) aim to protect benthic ecosystems (Hübner et al., 2009; Simpson and Batley, 2016). Assuming full

mixing in the top 10 cm of the sediment, up to 1.4 kg CKD or 74.8 kg LKD per m² could be applied to pristine sediments

without exceeding the strictest marine SQG of 30.2 mg kg^{-1} for Pb (Appendix C). Overall, these findings underscore the need

for ecotoxicological testing and cautious application of CKD to avoid ecological harm.

4.4 Longer term fate of unreacted phases

Both LKD and CKD contained a significant amount of unreactive phases (75 and 71 wt%, respectively) that remained inert

over the 15-day experimental time scale. In coastal and shelf environments, this residual material would rapidly settle to the

seafloor. The residual fraction consists primarily of $CaCO_3$ phases (52 % in CKD and 72 % in LKD). When mixed into the

seabed through local hydrodynamics and bioturbation, porewater acidification from microbial degradation of organic matter

415 can trigger metabolic $CaCO_3$ dissolution (Rao et al., 2012; Kessler et al., 2020). This process takes place under oxic conditions

and produces 2 moles of alkalinity per mole of dissolved $CaCO_3$.

$$CaCO_3 + CO_2 + H_2O \rightarrow Ca^{2+} + 2HCO_3^-$$ (6)

In anoxic environments, organic matter mineralization generates more A_T than DIC, quickly increasing Ω_{cal} and thereby inhibiting dissolution (Morse and Mackenzie, 1990; Burdige, 2006). If kiln dust OAE is applied to continental shelf waters lying above permeable marine sediments, weathering of all calcite in the residual kiln dust could additionally produce a maximum of 10.8 mmol A_T g^{-1} LKD and 7.4 mmol A_T g^{-1} CKD. However, large-scale fining of sediment with kiln dust could reduce the oxygen penetration depth, limiting the zone for metabolic $CaCO_3$ dissolution (Ahmerkamp et al., 2017). The potential for enhanced sedimentary alkalinity generation via residual kiln dust addition to permeable marine sediments therefore warrants further experimental investigation. If fully realized, the total alkalinity release potential (immediate dissolution and metabolic $CaCO_3$ dissolution) could reach up to 18.8 mmol g^{-1} for LKD and 9.8 mmol g^{-1} for CKD. By contrast, in open-ocean applications, the residual material would settle to the deep seafloor, where metabolic dissolution would occur in waters isolated from the atmosphere and thus would not contribute to CDR on relevant (year–decade) timescales.

4.5 Carbon dioxide removal potential

Achieving the Paris Agreement targets will require 12–15 Gt CO_2 $year^{-1}$ of carbon removal by 2100 (Rockström et al., 2017; Minx et al., 2018). Kiln dust dissolution in seawater could potentially be one contributing approach within a broader CDR portfolio. Short-term weathering of LKD and CKD in seawater produced up to 8.02 ± 0.53 and 2.38 ± 0.16 mol of alkalinity per kg of source material, respectively (Fig. 2C). On average, 1 mol of added alkalinity sequesters 0.84 mol CO_2 in surface ocean waters (Schulz et al., 2023), thus resulting in 297 ± 20 g CO_2 kg^{-1} LKD and 88 ± 6 g CO_2 kg^{-1} CKD. With current global annual production of approximately 29 Mt for LKD and 287 Mt for CKD (CEMBUREAU, 2024; USGS, 2025), their maximum carbon dioxide removal potential via dissolution in seawater, assuming an average of 0.07 t of kiln dust produced per tonne of lime or cement (Al-Refeai and Al-Karni, 1999), is approximately 8.7 ± 0.6 Mt CO_2 yr^{-1} for LKD and 25 ± 2 Mt CO_2 yr^{-1} for CKD. Additional CO_2 uptake through metabolic calcite dissolution in coastal and shelf sediments could potentially further increase this to 13.4 Mt yr^{-1} for LKD and 57 Mt yr^{-1} for CKD, although the effectiveness and time scaling of this process are uncertain. Cumulative this would amount to 1 Gt and 4.3 Gt CO_2 by 2100, assuming constant kiln dust production rates and complete utilization for OAE from 2025 onwards. While significant, this represents only 1.9–2.8 % of the 2.5–3.7 Gt CO_2

emitted annually by the cement and lime industries (Simoni et al., 2022; Cheng et al., 2023). Therefore, decarbonizing these sectors remains the top priority for effective climate change mitigation (Simoni et al., 2022; Barbhuiya et al., 2024).

The CDR estimates presented here are upper-bound values, assuming that all globally produced LKD and CKD will be used for OAE, and that production rates remain constant throughout the 21st century. In practice, some kiln dust will be used for

445 other economically viable applications (Al-Bakri et al., 2022), while on the other hand, cement demand is projected to increase by 12–23 % by 2050, which will increase kiln dust production (IEA, 2018). CO_2 emissions from transporting kiln dust to the ocean were not considered, but their impact on net CDR is likely minor if deployment occurs near production sites with minimal road transport (Foteinis et al., 2022). These CDR estimates also assume full atmospheric CO_2 equilibration of A_T-enriched surface waters ($\gamma_{CO_2} \approx 0.84$), while actual values in coastal regions are possibly lower ($\gamma_{CO_2} \approx 0.65 - 0.8$), due to

450 alkalinity transport to the deep ocean without prior atmospheric exchange (He and Tyka, 2023). Therefore, application should focus on continental shelf seas, especially those with carbonate-poor sediments (Lunstrum and Berelson, 2022), to promote metabolic $CaCO_3$ dissolution and maximize the CDR potential. Importantly, only one specific type of CKD and LKD were tested in this study, and mineralogical and chemical composition can vary significantly with the production process, thus affecting the CDR potential (Pavía and Regan, 2010; Siddique, 2014; Drapanauskaite et al., 2021). Tailoring application

455 concentrations to site-specific conditions and material properties is therefore essential for safe and effective deployment.


5   Conclusions

Cement kiln dust (CKD) and lime kiln dust (LKD) are abundant, fine-grained, and alkaline industrial byproducts available at low cost. We conducted laboratory experiments to evaluate their suitability as mineral-based OAE feedstocks. Reactive phases in CKD and LKD dissolved rapidly in seawater, with 65–92 % dissolving within 1 hour and complete reactive phase dissolution

460 within 24 hours. LKD generated up to 8.02 ± 0.53 mmol of alkalinity per g, compared to 2.38 ± 0.16 mmol g⁻¹ for CKD. Alkalinity consuming secondary aragonite precipitation was observed at saturation states ≥6.2, with a saturation state of ~5 identified as a safe threshold. Based on current global production (~29 Mt year⁻¹ for LKD and ~287 Mt year⁻¹ for CKD), the theoretical maximum CDR potential via dissolution in seawater is 8.7 ± 0.6 Mt CO_2 year⁻¹ for LKD and 25 ± 2 Mt CO_2 year⁻¹ for CKD. Turbidity increases from both LKD and CKD, and trace metal release from CKD, present potential environmental

465 risks. To minimize secondary mineral formation and ecological impacts, site-specific application concentrations should be determined through particle dispersal modelling that accounts for local hydrodynamic conditions. A large portion of both materials, 75 % of LKD and 71 % of CKD, remained undissolved, with calcite making up 72 % and 52 % of this residual fraction, respectively. If this residual calcite undergoes metabolic dissolution in marine sediments, it could further contribute to CDR, potentially adding up to 4.7 Mt CO_2 year^{-1} for LKD and 32 Mt CO_2 year^{-1} for CKD, although this requires further

470 experimental validation. Overall, LKD and, to a lesser extent, CKD show promise for OAE, with a CDR potential of up to 13.4 Mt year^{-1} for LKD and 57 Mt year^{-1} for CKD at current production levels.

Appendix A: Kiln dust properties

A1 Grain size, specific surface area, and elemental composition
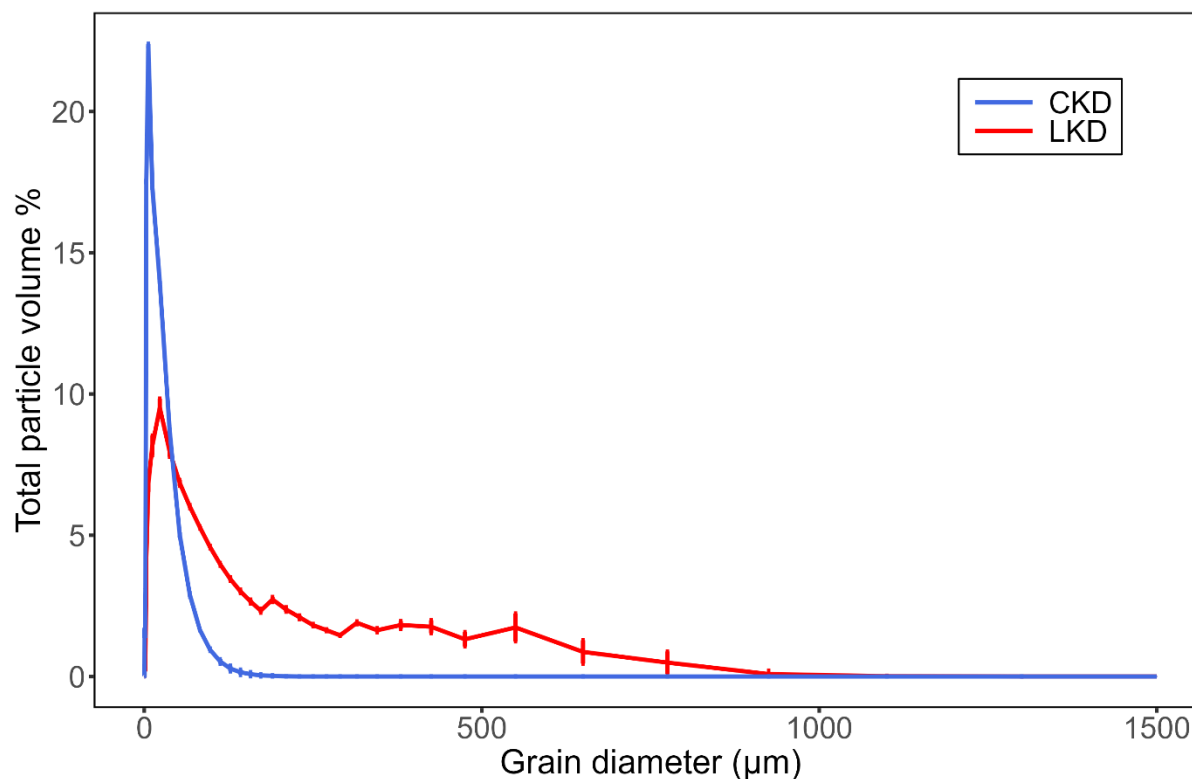
475

Figure A1: Volumetric grain size distribution of the fresh lime kiln dust (LKD, in red) and cement kiln dust (CKD, in red). Mean and standard deviation are shown (N = 3).

The geometric surface area A_{GEO} (m² g⁻¹) of the experimental kiln dusts is shown in Table 2 of the main text. It was calculated

480   from the different grain diameter classes i (n = 37, between 0.35 and 1300 µm grain diameter) of the volumetric particle size distribution (Fig. A1) as

$$A_{GEO} = \sum_{i=1}^{n} \left(\frac{\frac{V_{KD_i}}{V_{grain_i}} * A_{grain_i}}{\rho_{KD}} \right) \quad (1)$$

Where V_{KD_i} represents the relative volume (cm³ cm⁻³) for a certain grain diameter class i (e.g. 180 – 200 µm). V_{grain_i} and A_{grain_i} are the volume (cm³) and surface area (m²) of a single KD grain calculated from the average grain diameter of a certain

485   grain diameter class (e.g. 190 µm for 180 – 200 µm), assuming perfect spherical particles. ρ_{KD} is the specific gravity of the kiln dust (g cm⁻³).

Table A1: Elemental composition (wt%) of the cement kiln dust (CKD) and lime kiln dust (LKD). Concentrations were analysed via ICP-OES after heated digestion in a mixture of HClO₄, HNO₃, and HF as described in section 3.1 of the main text.

Element composition (wt%)	CKD	LKD
Al	3.02	0.038
As	<0.000016	<0.000016
Ba	0.044	0.00082
Be	0.000095	0.000012
Ca	27.8	44.9
Cd	0.0030	<0.00000085
Ce	0.0025	<0.0000028
Co	0.0015	<0.0000021
Cr	0.017	0.0011
Cu	0.028	0.0015
Fe	2.44	0.11
K	6.05	0.17
Li	0.0079	0.00025
Mg	0.57	0.22
Mn	0.11	0.0049
Mo	<0.0000082	<0.0000082
Na	1.22	0.080
Ni	0.011	<0.0000043
P	0.12	<0.000011
Pb	0.15	<0.000014
S	4.64	0.63
Sc	0.00046	<0.00000008
Sr	0.072	0.028
Ti	0.19	0.0013
V	0.036	0.00063
Y	0.0013	0.00016

Zn	0.65	0.0029

A2 Kiln dust settling time

To provide an initial simplified assessment of whether kiln dust particles could settle out of the ocean's mixed layer (assumed to be 200 m deep) before the complete dissolution of their reactive phases, Stokes' law (Eq. (2)) was applied to estimate their gravimetric settling velocity, assuming spherical particle geometry:

$$v = \frac{g d^2 (\rho_p - \rho_s)}{18 \eta} \tag{2}$$

where g is the acceleration of gravity (9.81 m² s⁻¹), d is the particle diameter (m), ρ_p is the density of the particle (2872 kg m⁻³ for LKD and 2712 kg m⁻³ for CKD), ρ_s is the density of the solution (1022 kg m⁻³ for 32 ‰ seawater at 20°C), and η is the dynamic viscosity of the solution (0.00108 kg m⁻¹ s⁻¹). Seawater density and dynamic viscosity were derived using the "swRho" and "swViscosity" function of the "oce" package in R. The settling time (h) required for particles to exit the mixed layer was calculated by dividing the mixed layer depth (200 m) by the settling velocity and converting the result from seconds to hours by multiplying by 3600.
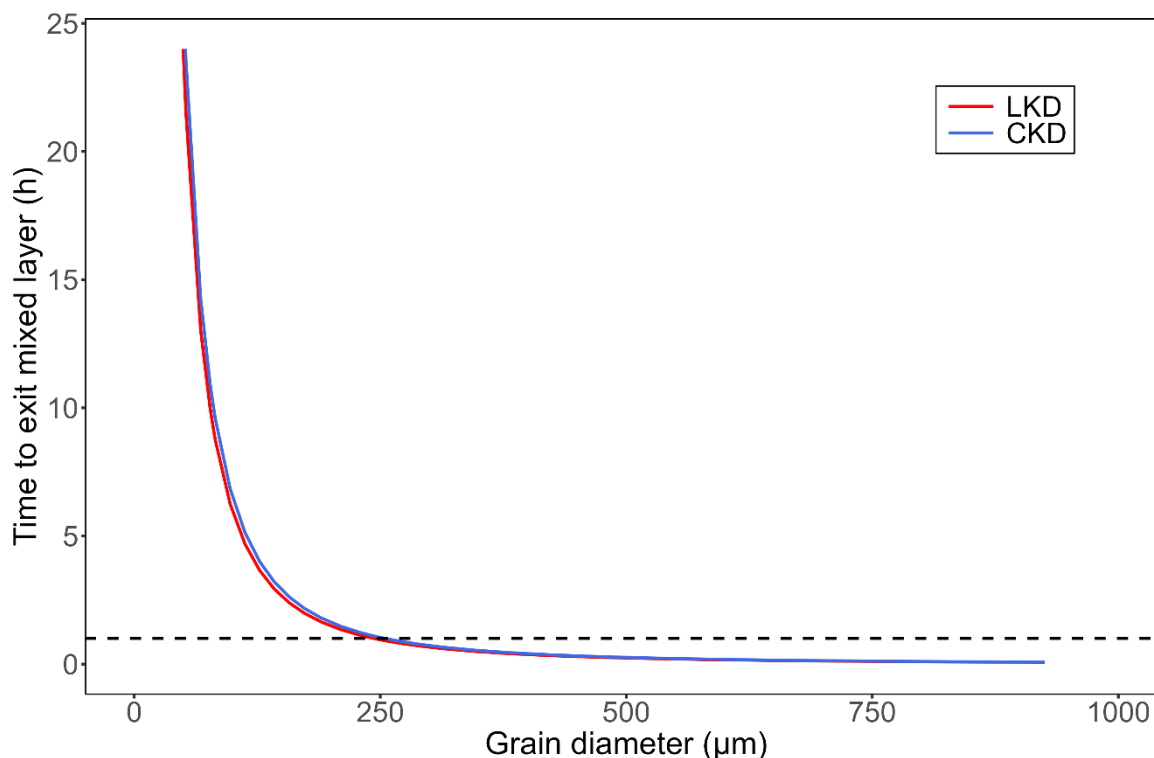
Figure A2: Expected time for perfectly spherical lime kiln dust (LKD, in red) and cement kiln dust (CKD, in blue) particles to sink below the mixed layer depth (assumed to be 200 m) according to Stokes' law. Horizontal black dashed line at represents the time (1 h) at which most (72 – 85%) reactive phases in LKD and CKD have dissolved.

27

After one hour of incubation at low application concentrations, most of the reactive phases in CKD ($72 \pm 12\%$) and LKD ($85 \pm 11\%$) had dissolved (Fig. 1B). Particles of LKD smaller than 244 µm and CKD smaller than 255 µm will remain suspended in the mixed layer for at least one hour (Fig. A2). Given the measured grain size distributions (Fig. A1), this means that 100% of CKD particles and $85 \pm 2\%$ of LKD particles would stay in the mixed layer for this duration.

510

A3 Residual kiln dust fraction experiment

Due to the limited remaining material (<70 mg) after the dissolution experiments presented in the main text, it was not possible to accurately quantify the residual mass of kiln dusts following dissolution in seawater. To address this, a separate small-scale test was conducted to determine the residual mass fraction. Two 2-liter plastic bottles were filled with 2 L of filtered seawater

515 and continuously aerated using air stones to speed up equilibration with atmospheric CO_2. Kiln dust was added to each bottle at concentrations of $87 \, \mathrm{mg\,kg^{-1}}$ for CKD and $21 \, \mathrm{mg\,kg^{-1}}$ for LKD, three times per day over the course of three consecutive days. Additions were spaced a minimum of 2.5 hours apart to avoid high pH increases that might induce secondary aragonite formation. After the final addition, the bottles were left to incubate at room temperature (16.1–17.5 °C) for 24 hours to ensure complete dissolution of the reactive phases. The suspensions were then filtered through pre-weighed dried (at 60 °C for 24 h)

520 0.3 µm pore size membrane filters (Seitz type M) using a Sartorius Microsart E-jet filtration unit. The filters were placed in pre-weighed Al foil cups, then dried at 60 °C for 72 hours, and subsequently reweighed using the same Mettler Toledo XP26 Excellence Plus microbalance to determine the residual solid mass. For LKD, the residual fraction was 75.42% of the added mass (379.28 mg), while for CKD, it was 70.58% of the added mass (1567.65 mg).

Appendix B: Seawater parameters experiment II
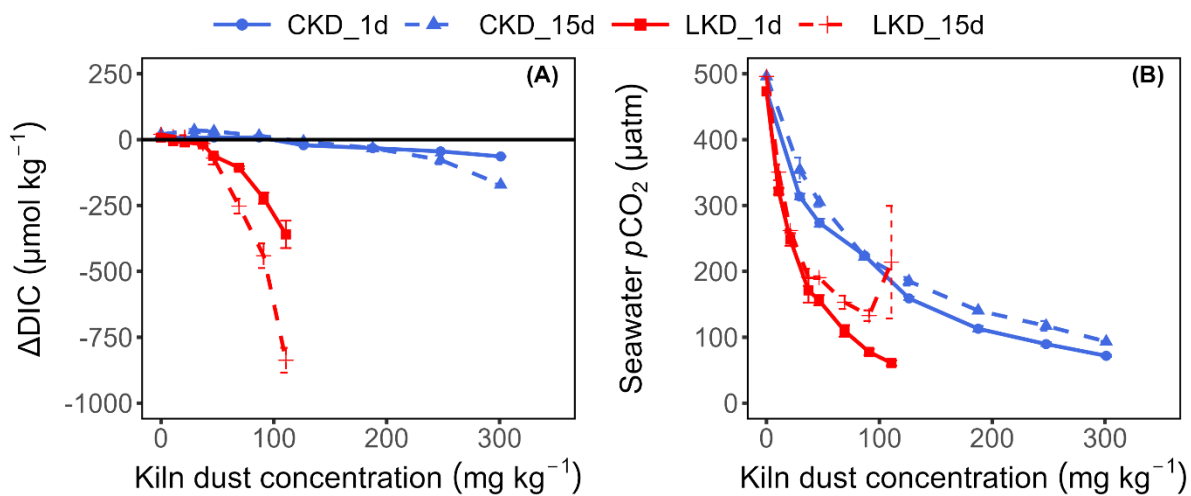
525 **B1 Observed seawater chemistry changes**

Figure B1. (A) Change in DIC concentration (µmol kg^{-1}) and (B) partial CO$_2$ pressure (pCO$_2$, expressed in µatm) as a function of the kiln dust application concentration (mg kg^{-1}) during dissolution experiment II. Results (as mean ± S.D., N=3) are shown for lime kiln dust (LKD, in red) and cement kiln dust (CKD, in blue) after 1 day (solid lines) or 15 days of incubation (dashed lines) in FSW.

530

29
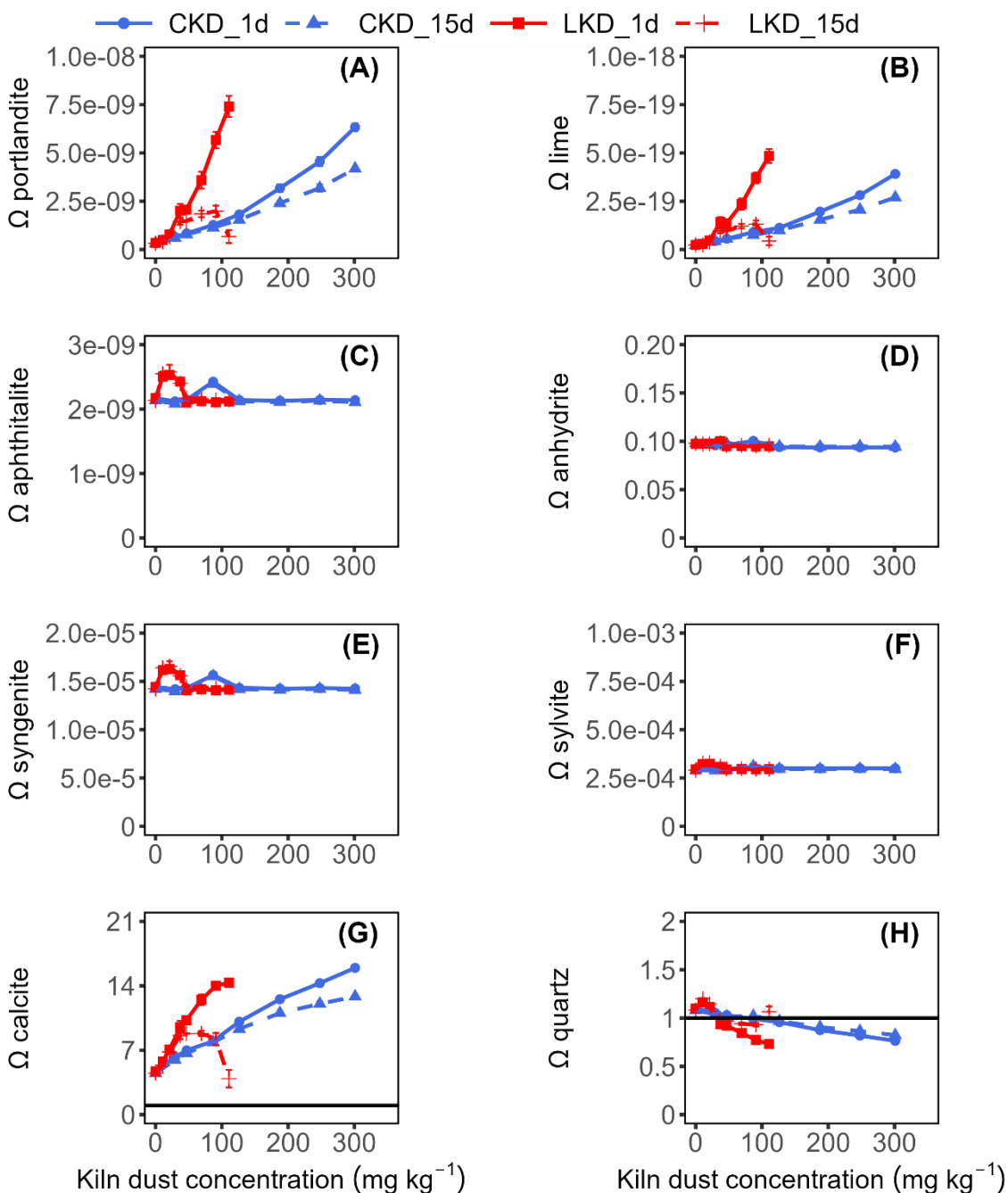
Figure B2. Saturation state (Ω) of (A) portlandite, (B) lime, (C) aphthitalite, (D) anhydrite, (E) syngenite, (F) sylvite, (G) calcite, and (H) quartz as a function of the kiln dust application concentration (mg kg^{-1}) during experiment II. Results (as mean ± S.D., N=3) are shown for lime kiln dust (LKD, in red) and cement kiln dust (CKD, in blue) after 1 day (solid lines) or 15 days of incubation (dashed lines) in FSW. The horizontal solid black line at Ω = 1 represents the critical saturation threshold.
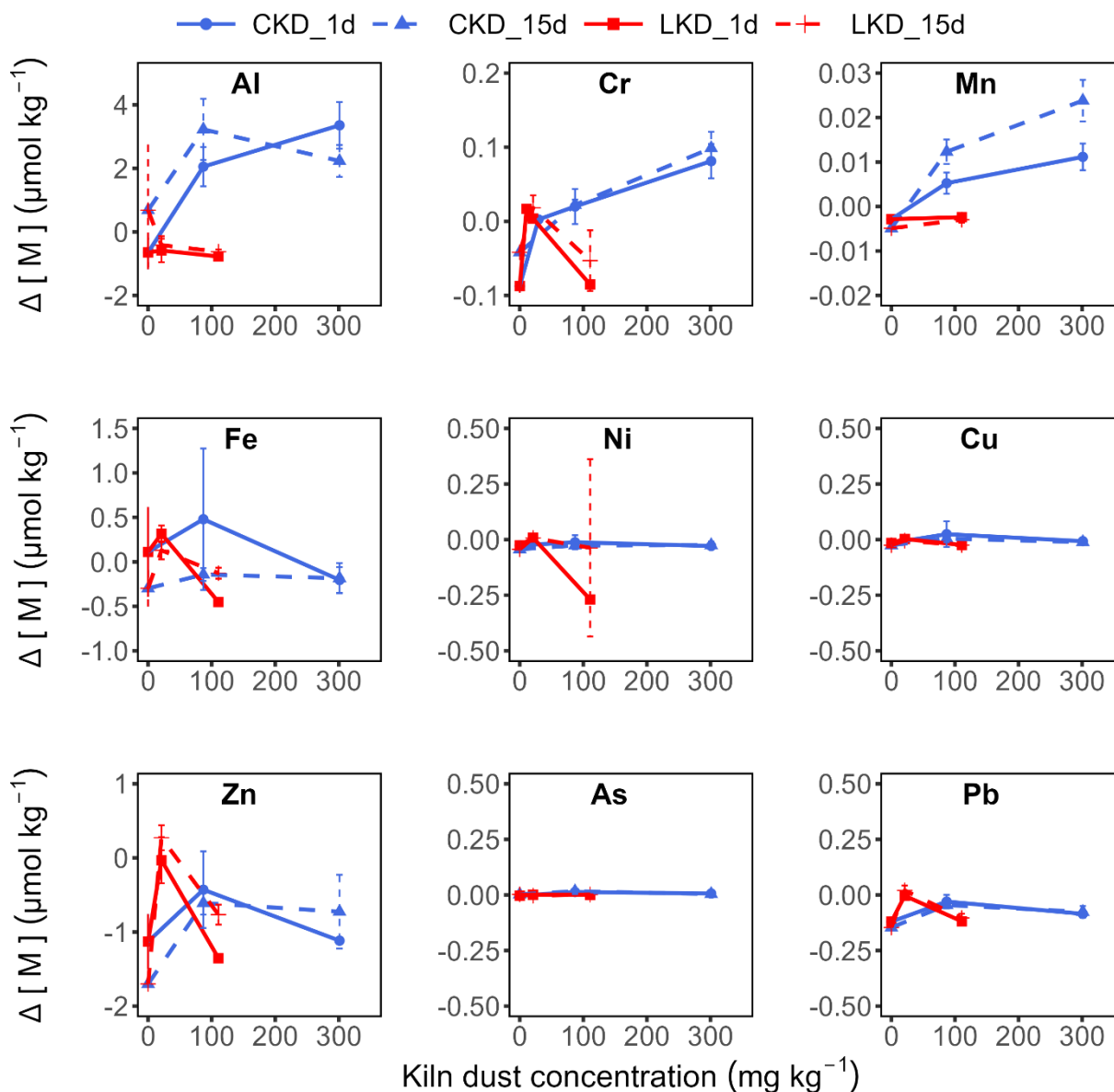
Figure B3: Metal(loid) accumulation in filtered seawater (µmol kg⁻¹) as a function of the kiln dust application concentration (mg kg⁻¹) during dissolution experiment II. The accumulation was calculated as the increase in metal(loid) concentrations above the initial seawater levels. Results (as mean ± S.D., N=3) are shown for lime kiln dust (LKD, in red) and cement kiln dust (CKD, in blue) after 1 day (solid lines) or 15 days of incubation (dashed lines) in FSW.

B2 Expected seawater trace metal accumulation

The expected accumulation ΔC_i (expressed in µmol kg^{-1}) of a given metal(loid) i in filtered seawater (FSW) under the

545   assumption of stoichiometric KD weathering was calculated from the measured total metal(loid) concentration χ (expressed in

mg kg^{-1}) in the KD and the dissolved KD fraction φ_{diss} (dimensionless) as follows:

$$\Delta C_i = \frac{m_{KD}\varphi_{diss}\chi}{m_{FSW}M_i} \tag{3}$$

Where m_{KD} and m_{FSW} reflect the masses (g) of kiln dust and filtered seawater, respectively, used in the plastic incubation

vials. M_i denotes the molar mass of a given metal(loid) i.
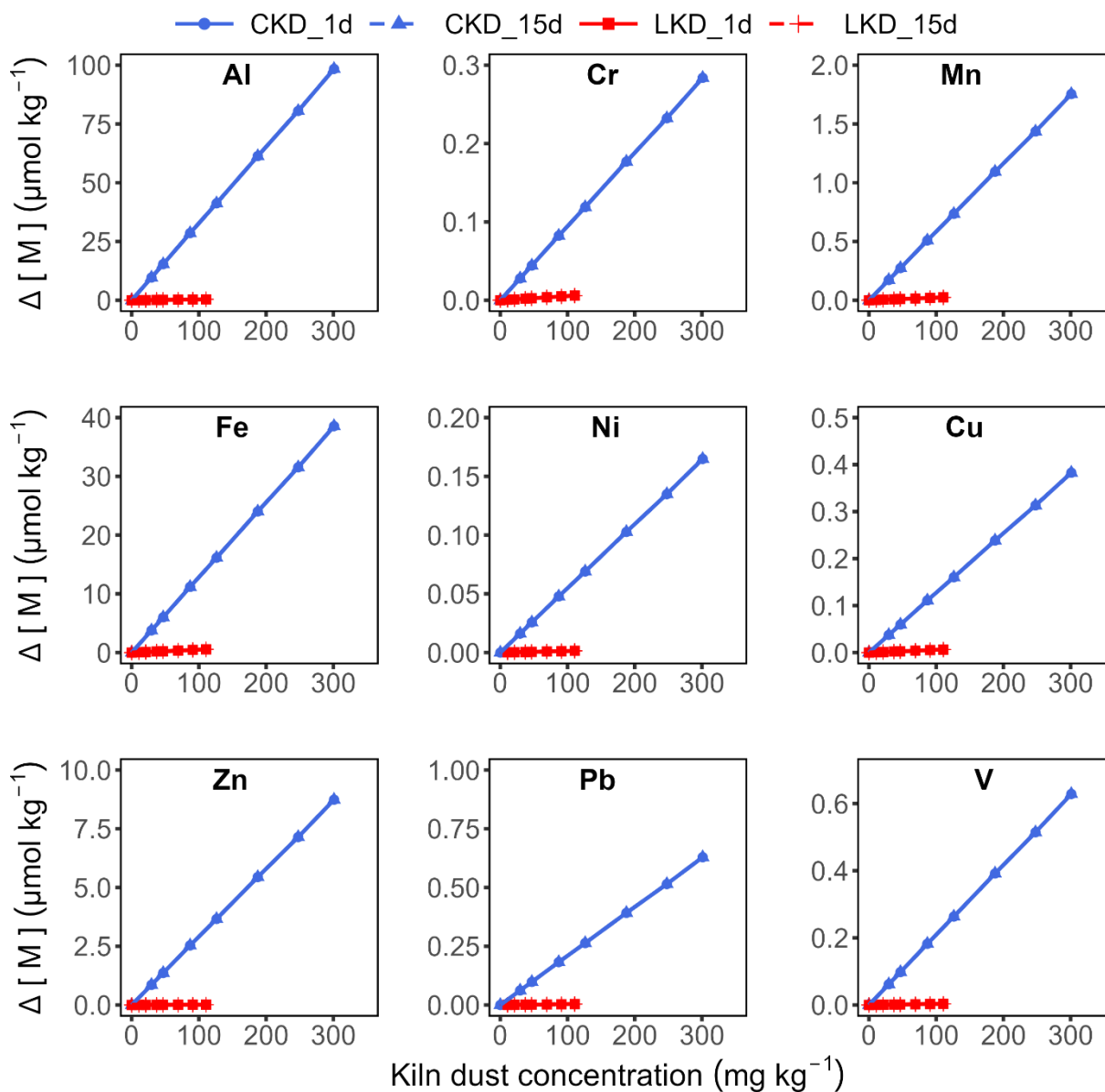
550

Figure B4. Expected metal(loid) accumulation in filtered seawater (μmol kg^{-1}) as a function of the kiln dust application concentration (mg kg^{-1}) during dissolution experiment II. Results are shown for lime kiln dust (LKD, in red) and cement kiln dust (CKD, in blue). Accumulation values after 1 day (solid lines) and 15 days (dashed lines) were assumed to be equal given that all total alkalinity producing reactive phase dissolution occurred within the first day.

555 **Appendix C: Maximum sedimentary kiln dust application concentration**

In real-world ship-based deployments, residual kiln dust (KD) would settle on the seafloor, where it would be mixed into the surface sediment through local hydrodynamics and bioturbation. This accumulation and possible subsequent dissolution of residual KD, could lead to the build-up of metals in the surface sediment, potentially posing a toxicological risk to benthic organisms. Sediment Quality Guidelines (SQGs) are employed to assess the risk of metal toxicity to marine biota in a tiered

560 approach, with the first step involving the comparison of total sediment metal concentrations to these guidelines (Hübner et al., 2009; Simpson and Batley, 2016). The kiln dust contain a range of metals (Appendix A Table A1) of which Pb could mostly easily exceed existing SGQs based on preliminary screening. Following Flipkens et al. (2021) we derived the maximum allowable KD application m_{app} (expressed in kg m^{-2} seafloor) that would not exceed marine Pb SQGs via:

$$m_{app} = \frac{(C_{SQG} - C_{bg}) V_s \rho_s (1 - \Phi)}{\chi} \qquad (4)$$

565 where C_{SQG} is the sediment quality guideline for Pb (mg kg^{-1} dry wt), C_{bg} is the background sedimentary Pb concentration (mg kg^{-1} dry wt), V_s is the volume of the sediment in which the kiln dust is mixed per m^2 of seabed (m^3 m^{-2} seabed), ρ_s is the specific density of marine sediment (2650 kg m^{-3}), Φ is the porosity of the sediment, and χ is the concentration of Pb (mg kg^{-1} dry wt) in CKD or LKD (Table A1). The porosity of marine surface sediment was assumed to be 0.60 based on the predicted global coastal sediment porosity ranging from approximately 0.50 to 0.85 (Martin et al., 2015). A sediment mixing depth of

570 10 cm was assumed, reflecting the typical depth where most benthic biota are found (Simpson and Batley, 2016; Solan et al., 2019). Given the global variation in Pb SQGs, maximum allowable KD application (m_{app}) calculations were made using different sediment quality guidelines, including the Chinese Interim Sediment Quality Guideline–Low (ISQV-low), the Australian Interim Sediment Quality Guideline–Low (ISQG-low), the Norwegian Predicted No Effect Concentration (PNEC), and the American Threshold Effect Level (TEL) (Hübner et al., 2009).
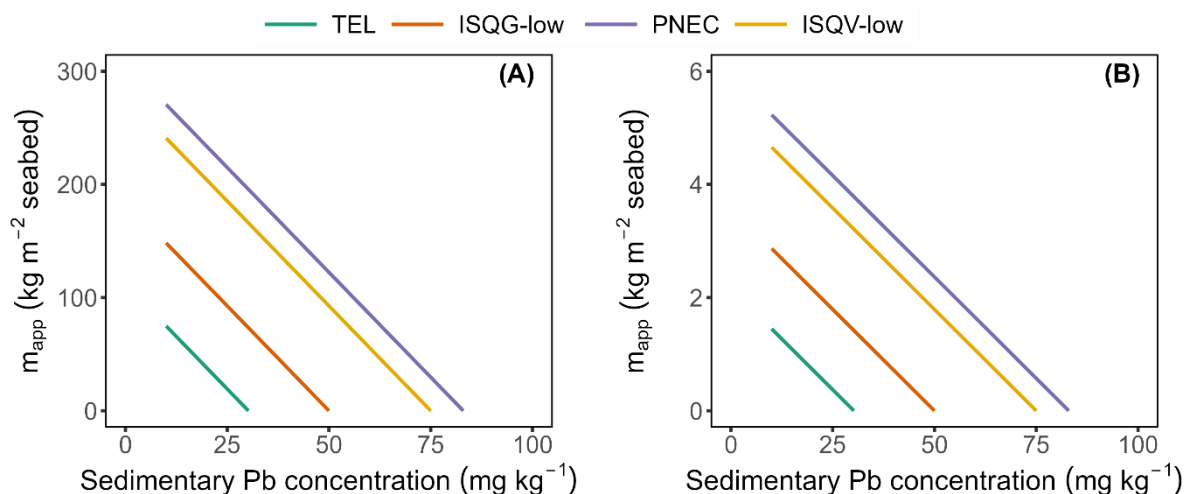
Figure C1: Maximum allowable application (m$_{app}$, expressed in kg m^{-2}) of (A) lime kiln dust or (B) cement kiln, without exceedance of lead (Pb) sediment quality guidelines (SQGs), plotted as a function of the background sedimentary Pb concentration (mg kg^{-1}). The considered SQGs include the Threshold Effect Level (TEL, green), the Interim Sediment Quality Guideline–low (ISQG-low, orange), the Predicted No Effect Concentration (PNEC, blue), and the Interim Sediment Quality Value–low (ISQV-low, yellow). A sediment mixing depth of 10 cm was assumed, and kiln dust Pb concentrations were based on measured values reported in Table A1. Results represent a conservative, worst-case scenario in which all Pb released during KD dissolution is retained within the sediment.

Code availability

The code used for analysis in this study is available upon request. Interested parties may contact the corresponding author.

Data availability

The data supporting the findings of this study have been deposited in Zenodo, DOI: https://doi.org/10.5281/zenodo.17174449. They are under embargo until the 1 June 2026, after which they will be publicly available. Reviewers have access via the following link: https://zenodo.org/records/17174450?token=eyJhbGciOiJIUzUxMiJ9.eyJpZCI6IjBmYWQxODBkLWRiZTItNDNkYy1iYmZmLTJjODJkZjZjNWFkZiIsImRhdGEiOnt9LCJyYW5kb20iOiI2MDUwYTgzYjE4ZTFlNDRlN2E0NDVjNGE2Y2UwNGNiNzkJ9.LbKTFMoy80SNuFdLtX2c8797cHhtKkoh-HH9XLRBS6bFxvMkveXWMVXlN5BEwDVRT43Kc_JcIF99FKThMv7PwA.

Author contribution

595 GF was responsible for conceptualization, data curation, formal analysis, investigation, methodology, visualization, writing original draft preparation, and writing review and editing. GF and GL carried out the investigation. FJRM was responsible for conceptualization, methodology, funding acquisition, resources, supervision, and writing review and editing.

Competing interests

The authors declare that they have no conflict of interest.

References

610 Ahmed, H. M., Hefni, M. A., Ahmed, H. A., Saleem, H. A.: Cement kiln dust (CKD) as a partial substitute for cement in pozzolanic concrete blocks, Buildings, 13, 568, https://doi.org/10.3390/buildings13020568, 2023.

Ahmerkamp, S., Winter, C., Krämer, K., Beer, D. d., Janssen, F., Friedrich, J., Kuypers, M. M., Holtappels, M.: Regulation of benthic oxygen fluxes in permeable sediments of the coastal ocean, Limnol. Oceanogr., 62, 1935-1954, https://doi.org/10.1002/lno.10544, 2017.

615 Al-Bakri, A. Y., Ahmed, H. M., Hefni, M. A.: Cement kiln dust (CKD): potential beneficial applications and eco-sustainable solutions, Sustainability, 14, 7022, https://doi.org/10.3390/su14127022, 2022.

Al-Refeai, T. O., Al-Karni, A. A.: Experimental study on the utilization of cement kiln dust for ground modification, Journal of King Saud University-Engineering Sciences, 11, 217-231, https://doi.org/10.1016/S1018-3639(18)30999-1, 1999.

ANZECC, ARMCANZ: Australian and New Zealand Guidelines for Fresh and Marine Water Quality. Retrieved from
620   https://www.waterquality.gov.au/sites/default/files/documents/anzecc-armcanz-2000-guidelines-vol1.pdf2000.

Arulrajah, A., Mohammadinia, A., D'Amico, A., Horpibulsuk, S.: Effect of lime kiln dust as an alternative binder in the stabilization of construction and demolition materials, Construction and Building Materials, 152, 999-1007, https://doi.org/10.1016/j.conbuildmat.2017.07.070, 2017.

Ayman, G., Shoaib, M., Balaha, M.: Thermo-chemical stability and mechanical properties of mortar made with cement kiln
625   dust-blended cement, Engineering Research Journal, 27, 49-58, https://erjm.journals.ekb.eg/article_82610_bc01c253b2da0256a63c6232f9fad8e0.pdf, 2004.

Bach, L. T., Gill, S. J., Rickaby, R. E., Gore, S., Renforth, P.: CO2 removal with enhanced weathering and ocean alkalinity enhancement: Potential risks and co-benefits for marine pelagic ecosystems, Front. clim., 1, 7, https://doi.org/10.3389/fclim.2019.00007, 2019.

630 Ban, C. C., Ee, T. L., Ramli, M., Akil, H. B. M., Mo, K. H.: Properties and microstructure of lime kiln dust activated slag-fly ash mortar, Construction and Building Materials, 347, 128518, https://doi.org/10.1016/j.conbuildmat.2022.128518, 2022.

Barbhuiya, S., Kanavaris, F., Das, B. B., Idrees, M.: Decarbonising cement and concrete production: Strategies, challenges and pathways for sustainable development, Journal of Building Engineering, 108861,
635   https://doi.org/10.1016/j.jobe.2024.108861, 2024.

Barnat-Hunek, D., Góra, J., Suchorab, Z., Łagód, G.: Cement kiln dust, Waste and Supplementary Cementitious Materials in Concrete, Elsevier, 149-180, https://doi.org/10.1016/B978-0-08-102156-9.00005-5, 2018.

Bell, J. J., McGrath, E., Biggerstaff, A., Bates, T., Bennett, H., Marlow, J., Shaffer, M.: Sediment impacts on marine sponges, Mar. Pollut. Bull., 94, 5-13, https://doi.org/10.1016/j.marpolbul.2015.03.030, 2015.

640 Beltagui, H., Sonebi, M., Maguire, K., Taylor, S.: Utilisation of cement kiln dust for the activation of fly ash in low strength applications, Academic Journal of Civil Engineering, 35, 549-553. 2017.

Bullock, L. A., James, R. H., Matter, J., Renforth, P., Teagle, D. A.: Global carbon dioxide removal potential of waste materials from metal and diamond mining, Front. clim., 3, 694175, https://doi.org/10.3389/fclim.2021.694175, 2021.

Bullock, L. A., Yang, A., Darton, R. C.: Kinetics-informed global assessment of mine tailings for CO2 removal, Sci. Total
645   Environ., 808, 152111, https://doi.org/10.1016/j.scitotenv.2021.152111, 2022.

Burdige, D.: Geochemistry of Marine Sediments, Princeton New Jersey, Princeton University Press, https://doi.org/10.1515/9780691216096, 2006.

Camatti, E., Valsecchi, S., Caserini, S., Barbaccia, E., Santinelli, C., Basso, D., Azzellino, A.: Short-term impact assessment of ocean liming: A copepod exposure test, Mar. Pollut. Bull., 198, 115833,
650   https://doi.org/10.1016/j.marpolbul.2023.115833, 2024.

Caserini, S., Pagano, D., Campo, F., Abbà, A., De Marco, S., Righi, D., Renforth, P., Grosso, M.: Potential of maritime transport for ocean liming and atmospheric CO2 removal, Front. clim., 3, 575900, https://doi.org/10.3389/fclim.2021.575900, 2021.

Caserini, S., Storni, N., Grosso, M.: The availability of limestone and other raw materials for ocean alkalinity enhancement,
655   Glob. Biogeochem. Cycles, 36, e2021GB007246, https://doi.org/10.1029/2021GB007246, 2022.

CEMBUREAU: The European cement association (Cembureau) 2023 activity report, https://cembureau.eu/media/dnbf4xzc/activity-report-2023-for-web.pdf, 2024.

Cheng, D., Reiner, D. M., Yang, F., Cui, C., Meng, J., Shan, Y., Liu, Y., Tao, S., Guan, D.: Projecting future carbon emissions from cement production in developing countries, Nat. Commun., 14, 8213, https://doi.org/10.1038/s41467-023-
660   43660-x, 2023.

Cheung, S., Shin, P.: Size effects of suspended particles on gill damage in green-lipped mussel Perna viridis, Mar. Pollut. Bull., 51, 801-810, https://doi.org/10.1016/j.marpolbul.2005.02.019, 2005.

Cloern, J. E.: Turbidity as a control on phytoplankton biomass and productivity in estuaries, Cont. Shelf Res., 7, 1367-1381, https://doi.org/10.1016/0278-4343(87)90042-2, 1987.

665 Collins, R. J., Emery, J.: Kiln dust-fly ash systems for highway bases and subbases, United States Department of Transportation - Federal Highway Administration.https://rosap.ntl.bts.gov/view/dot/41861, 1983.

Dale, A. W., Geilert, S., Diercks, I., Fuhr, M., Perner, M., Scholz, F., Wallmann, K.: Seafloor alkalinity enhancement as a carbon dioxide removal strategy in the Baltic Sea, Commun. Earth Environ., 5, 452, https://doi.org/10.1038/s43247-024-01569-3, 2024.

670 Dan-Asabe, B., Yaro, S., Yawas, D., Aku, S.: Water displacement and bulk density-relation methods of finding density of powdered materials, Int J of Innov Res in Sc, Eng and Tech, 2. 2013.

Dickson, A. G., Sabine, C. L., Christian, J. R.: Guide to best practices for ocean CO2 measurements, North Pacific Marine Science Organization, https://doi.org/10.25607/OBP-1342, 2007.

Drapanauskaite, D., Buneviciene, K., Repsiene, R., Mazeika, R., Navea, J., Baltrusaitis, J.: Physicochemical characterization
675   of pelletized lime kiln dust as potential liming material for acidic soils, Waste and Biomass Valorization, 12, 1267-1280, https://doi.org/10.1007/s12649-020-01107-0, 2021.

Dvorkin, L., Zhitkovsky, V.: Cement–ash concrete with the addition of lime kiln dust, Frontiers in Materials, 10, 1196407, https://doi.org/10.3389/fmats.2023.1196407, 2023.

Elbaz, A., Aboulfotoh, A., Dohdoh, A., Wahba, A.: Review of beneficial uses of cement kiln dust (CKD), fly ash (FA) and
680   their mixture, J. Mater. Environ. Sci, 10, 1062-1073. 2019.

Flipkens, G., Blust, R., Town, R. M.: Deriving nickel (Ni (II)) and chromium (Cr (III)) based environmentally safe olivine guidelines for coastal enhanced silicate weathering, Environ. Sci. Technol., 55, 12362-12371, https://doi.org/10.1021/acs.est.1c02974, 2021.

Flipkens, G., Fuhr, M., Fiers, G., Meysman, F. J., Town, R. M., Blust, R.: Enhanced olivine dissolution in seawater through
685   continuous grain collisions, Geochim. Cosmochim. Acta, 359, 84-99, https://doi.org/10.1016/j.gca.2023.09.002, 2023.

Foteinis, S., Andresen, J., Campo, F., Caserini, S., Renforth, P.: Life cycle assessment of ocean liming for carbon dioxide removal from the atmosphere, J. Clean. Prod., 370, 133309, https://doi.org/10.1016/j.jclepro.2022.133309, 2022.

Fuhr, M., Dale, A. W., Wallmann, K., Bährle, R., Kalapurakkal, H. T., Sommer, S., Spiegel, T., Dobashi, R., Buchholz, B.,
690   Schmidt, M.: Calcite is an efficient and low-cost material to enhance benthic weathering in shelf sediments of the Baltic Sea, Commun. Earth Environ., 6, 106, https://doi.org/10.1038/s43247-025-02079-6, 2025.

Geerts, L. J., Hylén, A., Meysman, F. J.: Review and syntheses: Ocean alkalinity enhancement and carbon dioxide removal through marine enhanced rock weathering using olivine, Biogeosciences, 22, 355-384, https://doi.org/10.5194/bg-22-355-2025, 2025.

695 He, J., Tyka, M. D.: Limits and CO 2 equilibration of near-coast alkalinity enhancement, Biogeosciences, 20, 27-43, https://doi.org/10.5194/bg-20-27-2023, 2023.

Hem, J. D.: Study and interpretation of the chemical characteristics of natural water, Department of the Interior, US Geological Survey, https://doi.org/10.3133/wsp2254, 1985.

Hofmann, A. F., Soetaert, K., Middelburg, J. J., Meysman, F. J.: AquaEnv: An Aquatic Acid–Base Modelling Environment in
700   R, Aquat. Geochem., 16, 507-546, https://doi.org/10.1007/s10498-009-9084-1, 2010.

Hübner, R., Astin, K. B., Herbert, R. J.: Comparison of sediment quality guidelines (SQGs) for the assessment of metal contamination in marine and estuarine environments, J. Environ. Monit., 11, 713-722, https://doi.org/10.1039/B818593J, 2009.

IEA: Cement technology roadmap plots path to cutting CO2 emissions 24% by 2050. https://www.iea.org/news/cement-
705   technology-roadmap-plots-path-to-cutting-co2-emissions-24-by-2050, Last access 18 September 2025, 2018.

IPCC: Climate Change 2023: Synthesis Report. Contribution of Working Groups I, II and III to the Sixth Assessment Report of the Intergovernmental Panel on Climate Change, IPCC.https://doi.org/10.59327/IPCC/AR6-9789291691647, 2023.

Kessler, A. J., Rogers, A., Cyronak, T., Bourke, M. F., Hasler-Sheetal, H., Glud, R. N., Greening, C., Meysman, F. J., Eyre,
710   B. D., Cook, P. L.: Pore water conditions driving calcium carbonate dissolution in reef sands, Geochim. Cosmochim. Acta, 279, 16-28, https://doi.org/10.1016/j.gca.2020.04.001, 2020.

Khanna, O. S.: Characterization and utilization of cement kiln dusts (CKDs) as partial replacements of Portland cement, Ph.D. thesis, University of Toronto, https://utoronto.scholaris.ca/server/api/core/bitstreams/58639a68-539a-4339-ae8d-f9b5181aaa64/content, 2010.

715 Kheshgi, H. S.: Sequestering atmospheric carbon dioxide by increasing ocean alkalinity, Energy, 20, 915-922, https://doi.org/10.1016/0360-5442(95)00035-F, 1995.

Kitidis, V., Rackley, S. A., Burt, W. J., Rau, G. H., Fawcett, S., Taylor, M., Tarran, G., Woodward, E. M. S., Harris, C., Fileman, T.: Magnesium hydroxide addition reduces aqueous carbon dioxide in wastewater discharged to the ocean, Commun. Earth Environ., 5, 354, https://doi.org/10.1038/s43247-024-01506-4, 2024.

720 Köhler, P., Abrams, J. F., Völker, C., Hauck, J., Wolf-Gladrow, D. A.: Geoengineering impact of open ocean dissolution of olivine on atmospheric CO2, surface ocean pH and marine biology, Environ. Res. Lett., 8, 014009, https://doi.org/10.1088/1748-9326/8/1/014009, 2013.

Latif, M. A., Naganathan, S., Razak, H. A., Mustapha, K. N.: Performance of lime kiln dust as cementitious material, Procedia Engineering, 125, 780-787, https://doi.org/10.1016/j.proeng.2015.11.135, 2015.

725 Lee, A.: North Sea: physical oceanography, Elsevier Oceanogr Ser, Elsevier, 467-493, https://doi.org/10.1016/S0422-9894(08)71359-X, 1980.

Lee, W.-S., Choi, Y.-C.: Hydration and Mechanical Properties of Cement Kiln Dust-Blended Cement Composite, Materials, 17, 4841, https://doi.org/10.3390/ma17194841, 2024.

Liu, X., Dunne, J. P., Stock, C. A., Harrison, M. J., Adcroft, A., Resplandy, L.: Simulating Water Residence Time in the
730 Coastal Ocean: A Global Perspective, Geophys. Res. Lett., 46, 13910-13919, https://doi.org/10.1029/2019GL085097, 2019.

Lowe, M., Morrison, M., Taylor, R.: Harmful effects of sediment-induced turbidity on juvenile fish in estuaries, Mar. Ecol. Prog. Ser., 539, 241-254, https://doi.org/10.3354/meps11496, 2015.

Lunstrum, A., Berelson, W.: CaCO3 dissolution in carbonate-poor shelf sands increases with ocean acidification and porewater
735 residence time, Geochim. Cosmochim. Acta, 329, 168-184, https://doi.org/10.1016/j.gca.2022.04.031, 2022.

Lunt, J., Smee, D. L.: Turbidity alters estuarine biodiversity and species composition, ICES Journal of Marine Science, 77, 379-387, https://doi.org/10.1093/icesjms/fsz214, 2020.

Martin, K. M., Wood, W. T., Becker, J. J.: A global prediction of seafloor sediment porosity using machine learning, Geophys. Res. Lett., 42, 10640-10646. 2015.

740 Minx, J. C., Lamb, W. F., Callaghan, M. W., Fuss, S., Hilaire, J., Creutzig, F., Amann, T., Beringer, T., de Oliveira Garcia, W., Hartmann, J.: Negative emissions—Part 1: Research landscape and synthesis, Environ. Res. Lett., 13, 063001, https://doi.org/10.1088/1748-9326/aabf9b, 2018.

Montserrat, F., Renforth, P., Hartmann, J., Leermakers, M., Knops, P., Meysman, F. J.: Olivine dissolution in seawater: implications for CO2 sequestration through enhanced weathering in coastal environments, Environ. Sci. Technol.,
745 51, 3960-3972, https://doi.org/10.1021/acs.est.6b05942, 2017.

Moras, C. A., Bach, L. T., Cyronak, T., Joannes-Boyau, R., Schulz, K. G.: Ocean alkalinity enhancement–avoiding runaway CaCO₃ precipitation during quick and hydrated lime dissolution, Biogeosciences, 19, 3537-3557, https://doi.org/10.5194/bg-19-3537-2022, 2022.

Moras, C. A., Joannes-Boyau, R., Bach, L. T., Cyronak, T., Schulz, K. G.: Carbon dioxide removal efficiency of iron and steel
750 slag in seawater via ocean alkalinity enhancement, Front. clim., 6, 1396487, https://doi.org/10.3389/fclim.2024.1396487, 2024.

Morse, J. W., Mackenzie, F. T.: Geochemistry of sedimentary carbonates, Elsevier, https://www.sciencedirect.com/bookseries/developments-in-sedimentology/vol/48/suppl/C, 1990.

Nikolov, A., Kostov-Kytin, V., Tarassov, M., Tsvetanova, L., Jordanov, N. B., Karamanova, E., Rostovsky, I.:
755 Characterization of cement kiln dust from Bulgarian cement plants, Journal of Chemical Technology and Metallurgy (JCTM), 60, 455-463, https://doi.org/10.59957/jctm.v60.i3.2025.11, 2025.

Nyström, E., Kaasalainen, H., Alakangas, L.: Prevention of sulfide oxidation in waste rock by the addition of lime kiln dust, Environ. Sci. Pollut. Res., 26, 25945-25957, https://doi.org/10.1007/s11356-019-05846-z, 2019.

Pan, Y., Li, Y., Ma, Q., He, H., Wang, S., Sun, Z., Cai, W.-J., Dong, B., Di, Y., Fu, W.: The role of Mg2+ in inhibiting CaCO3
760 precipitation from seawater, Mar. Chem., 237, 104036, https://doi.org/10.1016/j.marchem.2021.104036, 2021.

Parkhurst, D. L., Appelo, C.: Description of input and examples for PHREEQC version 3—a computer program for speciation, batch-reaction, one-dimensional transport, and inverse geochemical calculations, US geological survey techniques and methods, 6, 497, https://doi.org/10.3133/tm6A43, 2013.

Pavía, S., Regan, D.: Influence of cement kiln dust on the physical properties of calcium lime mortars, Mater. Struct., 43, 381-
765 391, https://doi.org/10.1617/s11527-009-9496-9, 2010.

38

Pedersen, M. F., Hansen, P. J.: Effects of high pH on a natural marine planktonic community, Mar. Ecol. Prog. Ser., 260, 19-31, https://doi.org/10.3354/meps260019, 2003.

R Core Team: R: A language and environment for statistical computing., R foundation for statistical computing http://www.R-project.org/, 2022.

770   Rao, A. M., Polerecky, L., Ionescu, D., Meysman, F. J., De Beer, D.: The influence of pore-water advection, benthic photosynthesis, and respiration on calcium carbonate dynamics in reef sands, Limnol. Oceanogr., 57, 809-825, https://doi.org/10.4319/lo.2012.57.3.0809, 2012.

Renforth, P., Henderson, G.: Assessing ocean alkalinity for carbon sequestration, Rev. Geophys., 55, 636-674, https://doi.org/10.1002/2016RG000533, 2017.

775   Renforth, P., Jenkins, B., Kruger, T.: Engineering challenges of ocean liming, Energy, 60, 442-452, https://doi.org/10.1016/j.energy.2013.08.006, 2013.

Rockström, J., Gaffney, O., Rogelj, J., Meinshausen, M., Nakicenovic, N., Schellnhuber, H. J.: A roadmap for rapid decarbonization, Science, 355, 1269-1271, https://doi.org/10.1126/science.aah3443, 2017.

Santinelli, C., Valsecchi, S., Retelletti Brogi, S., Bachi, G., Checcucci, G., Guerrazzi, M., Camatti, E., Caserini, S., Azzellino, 780   A., Basso, D.: Ocean liming effects on dissolved organic matter dynamics, Biogeosciences, 21, 5131-5141, https://doi.org/10.5194/bg-21-5131-2024, 2024.

Schulz, K. G., Bach, L. T., Dickson, A. G.: Seawater carbonate chemistry considerations for ocean alkalinity enhancement research: theory, measurements, and calculations, State Planet: SP, 2, 1-14. 2023.

Siddique, R.: Utilization of industrial by-products in concrete, Procedia Engineering, 95, 335-347, 785   https://doi.org/10.1016/j.proeng.2014.12.192, 2014.

Siddique, R., Rajor, A.: Use of cement kiln dust in cement concrete and its leachate characteristics, Resources, Conservation and Recycling, 61, 59-68, https://doi.org/10.1016/j.resconrec.2012.01.006, 2012.

Simoni, M., Wilkes, M. D., Brown, S., Provis, J. L., Kinoshita, H., Hanein, T.: Decarbonising the lime industry: State-of-the-art, Renewable and Sustainable Energy Reviews, 168, 112765, https://doi.org/10.1016/j.rser.2022.112765, 2022.

790   Simpson, S. L., Batley, G. E.: Sediment quality assessment: a practical guide, CSIRO Publishing, ISBN 978-1-486-30384-7, 2016.

Singleton, H.: Ambient Water Quality Guidelines (Criteria) for Turbidity, Suspended and Benthic Sediments: Overview Report, British Columbia Ministry of Water, Land, and Air Protection.https://www2.gov.bc.ca/assets/gov/environment/air-land-water/water/waterquality/water-quality-795   guidelines/approved-wqgs/bc_env_turbidity_waterqualityguideline_overview.pdf, 2021.

Solan, M., Ward, E. R., White, E. L., Hibberd, E. E., Cassidy, C., Schuster, J. M., Hale, R., Godbold, J. A.: Worldwide measurements of bioturbation intensity, ventilation rate, and the mixing depth of marine sediments, Sci. Data, 6, 1-6, https://doi.org/10.1038/s41597-019-0069-7, 2019.

Sreekrishnavilasam, A., King, S., Santagata, M.: Characterization of fresh and landfilled cement kiln dust for reuse in 800   construction applications, Engineering Geology, 85, 165-173, https://doi.org/10.1016/j.enggeo.2005.09.036, 2006.

Strydom, C., Roode, Q., Potgieter, J.: Thermogravimetric and X-ray powder diffraction analysis of precipitator dust from a rotating lime kiln, Cem. Concr. Res., 26, 1269-1276, https://doi.org/10.1016/0008-8846(96)00096-8, 1996.

Suitner, N., Faucher, G., Lim, C., Schneider, J., Moras, C. A., Riebesell, U., Hartmann, J.: Ocean alkalinity enhancement approaches and the predictability of runaway precipitation processes: results of an experimental study to determine 805   critical alkalinity ranges for safe and sustainable application scenarios, Biogeosciences, 21, 4587-4604, https://doi.org/10.5194/bg-21-4587-2024, 2024.

Sulpis, O., Jeansson, E., Dinauer, A., Lauvset, S. K., Middelburg, J. J.: Calcium carbonate dissolution patterns in the ocean, Nat. Geosci., 14, 423-428. 2021.

Tulcan, R. X. S., Ouyang, W., Lin, C., He, M., Wang, B.: Vanadium pollution and health risks in marine ecosystems: 810   Anthropogenic sources over natural contributions, Water Research, 207, 117838, https://doi.org/10.1016/j.watres.2021.117838, 2021.

USGS: Lime Statistics and Information. https://pubs.usgs.gov/periodicals/mcs2025/mcs2025-lime.pdf, Last access 11 April 2025, 2025.

Varliero, S., Buono, A., Caserini, S., Raos, G., Macchi, P.: Chemical Aspect of Ocean Liming for CO2 Removal: Dissolution
815　　　　Kinetics of Calcium Hydroxide in Seawater, ACS Engineering Au, 4, 422-431,
https://doi.org/10.1021/acsengineeringau.4c00008, 2024.

Yang, A. J., Timmermans, M.-L.: Assessing the effective settling of mineral particles in the ocean with application to ocean-based carbon-dioxide removal, Environ. Res. Lett., 19, 024035, https://doi.org/10.1088/1748-9326/ad2236, 2024.